1 **TITLE**

2 Precise Therapeutic Targeting of Distinct *NRXN1*$^{+/-}$ Mutations

3 **AUTHORS**

4 Michael B. Fernando[1,2,4,5], Yu Fan[3]*, Yanchun Zhang[3]*, Sarah Kammourh[3], Aleta N. Murphy[1,2,4],
5 Sadaf Ghorbani[5,6], Ryan Onatzevitch[2], Adriana Pero[3], Christopher Padilla[3], Erin K. Flaherty[1,2], Iya
6 K. Prytkova[2], Lei Cao[3], Sarah Williams[1-4], Gang Fang[3#], Paul A. Slesinger[2#] & Kristen J.
7 Brennand[2-5#]

8 **AFFILIATIONS**

9 [1] Graduate School of Biomedical Science, Icahn School of Medicine at Mount Sinai, New York,
10 NY 10029

11 [2] Nash Family Department of Neuroscience, Icahn School of Medicine at Mount Sinai, New York,
12 NY 10029

13 [3]Department of Genetics and Genomics, Icahn School of Medicine at Mount Sinai, New York, NY
14 10029

15 [4]Friedman Brain Institute, Black Family Stem Cell Institute, Pamela Sklar Division of Psychiatric
16 Genomics, Icahn School of Medicine at Mount Sinai, New York, NY 10029

17 [5] Department of Psychiatry, Yale School of Medicine, New Haven, CT, 06520

18 [6]Haukeland University Hospital, Bergen, Norway

19 *These authors contributed equally

20 [#]Correspondence: kristen.brennand@yale.edu, paul.slesinger@mssm.edu and
21 gang.fang@mssm.edu

22 **KEYWORDS**

23 Human induced pluripotent stem cells; *NRXN1*; alternative splicing; glutamatergic neurons;
24 GABAergic neurons; genomics; neuropsychiatric disorder; disease modeling; precision medicine

ABSTRACT

As genetic studies continue to identify risk loci that are significantly associated with risk for neuropsychiatric disease, a critical unanswered question is the extent to which diverse mutations --sometimes impacting the same gene-- will require tailored therapeutic strategies. Here we consider this in the context of rare neuropsychiatric disorder-associated copy number variants (2p16.3) resulting in heterozygous deletions in *NRXN1*, a pre-synaptic cell adhesion protein that serves as a critical synaptic organizer in the brain. Complex patterns of *NRXN1* alternative splicing are fundamental to establishing diverse neurocircuitry, vary between the cell types of the brain, and are differentially impacted by unique (non-recurrent) deletions. We contrast the cell-type-specific impact of patient-specific mutations in *NRXN1* using human induced pluripotent stem cells, finding that perturbations in *NRXN1* splicing result in divergent cell-type-specific synaptic outcomes. Via distinct loss-of-function (LOF) and gain-of-function (GOF) mechanisms, *NRXN1*$^{+/-}$ deletions cause decreased synaptic activity in glutamatergic neurons, yet increased synaptic activity in GABAergic neurons. Stratification of patients by LOF and GOF mechanisms will facilitate individualized restoration of *NRXN1* isoform repertoires; towards this, antisense oligonucleotides knockdown mutant isoform expression and alters synaptic transcriptional signatures, while treatment with β-estradiol rescues synaptic function in glutamatergic neurons. Given the increasing number of mutations predicted to engender both LOF and GOF mechanisms in brain disease, our findings add nuance to future considerations of precision medicine.

MAIN

Neurexins are pre-synaptic cell adhesion proteins that act as a synaptic organizer[1]. There are three neurexin genes (*NRXN1*, *NRXN2*, and *NRXN3*) in mammals and each is highly alternatively spliced to produce hundreds of isoforms, primarily categorized into long alpha and shorter beta isoforms[2]. The complex alternative splicing of neurexins allows for widespread expansion of protein-protein interaction capabilities[3], providing the basis for neurexins to interact with diverse post-synaptic ligands to establish and maintain neurotransmission. *NRXN1*α splice variants are specific to brain regions[4] and between cell types[5], but the cell-type-specific functional impact of individual isoforms remains unclear. Although rare in the population, large copy number variations (deletions or duplications) at the *NRXN1* locus 2p16.3, particularly those deleting exonic regions are highly penetrant, pleiotropic, and are strongly associated with several neuropsychiatric diseases, including schizophrenia (odds ratio 14.4(ref. [6]), autism spectrum disorder (odds ratio 14.9ref. [7]), epilepsy (odds ratio 9.91ref. [8]), intellectual disability (odds ratio 7.47ref. [9]) and

57 Tourette's syndrome (odds ratio 20.3ref. [10]). These exonic deletions in *NRXN1* are non-recurrent
58 (that is, they vary in size and location), making it difficult to determine the molecular mechanisms
59 underlying their diverse clinical symptoms (e.g., diagnosis, severity, prognosis, and age-of-onset).
60 In rodent studies, gene knock outs (KO) of *NRXNs* is sufficient to produce an array of excitatory
61 and inhibitory synaptic phenotypes[1]. However, heterozygous KO produce modest behavioral and
62 physiological changes *in-vivo*[11]. By contrast, however, *in-vitro* studies of engineered heterozygous
63 *NRXN1*$^{+/-}$ human neurons reveal robust changes in excitatory neurotransmission that are not
64 observed in matched *NRXN1*$^{+/-}$ mouse neurons[12,13]. While these studies do not evaluate how
65 *NRXN1*$^{+/-}$ impacts the complex alternative splicing of the gene or the non-recurrent nature of the
66 deletions, they collectively suggest that neurexins possess unique human neurobiology, and
67 therefore, the impact of the distinct patient-specific *NRXN1*$^{+/-}$ must be specifically evaluated in
68 human models.

69 Human induced pluripotent stem cell (hiPSC)-derived neurons provide an ideal platform to study
70 *NRXN1α* alternative splicing. Previously we established that hiPSC-derived forebrain cultures,
71 comprised of a mixture of glutamatergic and GABAergic neurons with astroglia, recapitulate the
72 diversity of *NRXN1α* alternative splicing observed in the human brain, cataloguing 123 high-
73 confidence *NRXN1α* isoforms[14]. Furthermore, using patient-derived *NRXN1*$^{+/-}$ hiPSCs with unique
74 5' or 3' deletions in the gene, we uncovered wide-scale reduction in wildtype *NRXN1α* isoform
75 levels and, robust expression of dozens of novel isoforms from the 3' mutant allele[14].
76 Overexpression of individual wildtype isoforms ameliorated reduced neuronal activity in patient-
77 derived *NRXN1*$^{+/-}$ hiPSC-neurons in a genotype-dependent manner, whereas mutant isoform
78 expression decreased neuronal activity levels in control hiPSC-neurons[14]. We therefore
79 hypothesized that 5' deletions of the promoter region represent classical loss-of-function (LOF),
80 while robust expression of 3' specific novel mutant isoforms confer a gain-of-function (GOF) effect
81 that cannot be rescued by overexpression of wildtype isoforms. Although *NRXN1* splicing varies
82 between the cell types of the brain, the impact of non-recurrent *NRXN1*$^{+/-}$ deletions on cell-type-
83 specific splicing patterns and synaptic function remains untested.

84 Neurexin signaling impacts both glutamatergic and GABAergic synapse properties[15,16],
85 suggesting that neurexins may regulate excitatory and inhibitory balance, which is strongly
86 implicated across neuropsychiatric disorders [17]. Given its multifaceted roles, the lack of
87 mechanistic understanding of how aberrant *NRXN1* splicing impacts neuronal physiology in a
88 cell-type *and* genotype-dependent manner presents a significant challenge for therapeutic
89 targeting. To discover the disease mechanisms that underpin *NRXN1*$^{+/-}$ deletions, we leverage

90 advanced 2D lineage conversion, and 3D organoid models to simultaneously compare excitatory
91 and inhibitory neurons, across 5' LOF and 3' GOF deletions. Our experiments were conducted
92 with separate populations of glutamate and GABA neurons, to specifically evaluate cell-
93 autonomous phenotypes arising from distinct *NRXN1*$^{+/-}$ deletions. We identified points of
94 phenotypic divergence across glutamatergic and GABAergic neurons, which were independently
95 validated in isogenic experiments to establish causal relationships between aberrant splicing and
96 synaptic dysfunction. Finally, we inform and test the design of novel therapeutic agents for
97 *NRXN1*$^{+/-}$ deletions on LOF/GOF stratified patient mechanisms.

98 **RESULTS**

99 **Shared aberrant splicing in patient-specific glutamatergic and GABAergic neurons.**

100 To examine the impact of *NRXN1*$^{+/-}$ deletions in two different neuronal cell types, we used lineage
101 conversion of patient hiPSCs for generating either excitatory glutamatergic neurons or inhibitory
102 GABAergic neurons. Transient overexpression of *NGN2* in hiPSCs produces iGLUT neurons that
103 are >95% pure glutamatergic neurons, robustly express glutamatergic genes, release glutamate,
104 and produce spontaneous synaptic activity by day 21 in vitro[18-21]. On the other hand, transient
105 overexpression of *ASCL1* and *DLX2* yields iGABA neurons that are >80% positive for expressing
106 GABA and GAD1/2 by day 35 in vitro, and possess mature physiologic properties of inhibitory
107 neurons by day 42[19,22]. We applied these highly efficient iGLUT and iGABA induction protocols
108 to hiPSCs from patients with rare heterozygous intragenic deletions in *NRXN1*[14]. Two cases
109 containing the same ~136-kb deletion in the 3'-region of *NRXN1* (3'-Del) and two cases with ~115-
110 kb deletions in the 5'-region of *NRXN1* (5'-Del). For controls, we used passage-matched hiPSCs
111 from four healthy sex-balanced subjects (**Fig. 1a,b**). Immunostaining confirmed expression of
112 neurotransmitter transporters, vGLUT1 and vGAT for iGLUT and iGABA neurons, respectively
113 (**Fig. 1c,h**). RNA-sequencing (RNAseq) further validated iGLUT (DIV21) and iGABA (DIV35)
114 neuronal induction in all donors (**Fig. 1d,i**).

115 We first compared the transcriptomics of *NRXN1*$^{+/-}$ deletions with controls for both iGLUT and
116 iGABA neurons. RNAseq analyses revealed overlap of the top differentially expressed genes
117 (DEGs) across cell types/genotypes (e.g., *FAM66D, TTC34, GALNT9*), whereas the majority of
118 case/control DEGs were genotype-specific (**Fig. 1e,j**). Gene-ontology analyses revealed a robust
119 enrichment of developmental and synaptic terms for the 5'-Del iGLUT condition over all other
120 conditions (**Supplementary Table S1**). Using publicly curated gene lists[23,24], risk enrichments for

121 schizophrenia, bipolar disorder, and autism spectrum disorder were most enriched in iGLUT
122 neurons from 5'-Del cases and iGABA neurons from 3'-Del cases (**Fig. 1f,k and Extended Data**
123 **Fig. 2**). Baseline transcriptional comparisons therefore suggested the potential of strong
124 phenotypes for 5'-Del iGLUT neurons. Despite cell-type-specific *NRXN1* isoform profiles reported
125 in healthy brains[5] and neurons[14], aberrant *NRXN1* alpha/beta exon usages were shared between
126 *NRXN1*$^{+/-}$ iGLUT and iGABA neurons (**Fig. 1g,l**), whereby alpha exon usage decreased for 5'-Del
127 and increased for 3'-Del in both types of neurons. These observations with specific iGLUT and
128 iGABA neurons parallel those from our previous study using hiPSC-derived forebrain neurons,
129 which was a mixture of glutamatergic and GABAergic neurons with astroglia[14].

130 **Patient-specific alterations in spontaneous neural activity occur without changes in**
131 **passive and excitable membrane properties.**

132 To evaluate the functional consequence of *NRXN1*$^{+/-}$ deletions on neuronal activity, we conducted
133 a population-level analysis of spontaneous neuronal activity using a multi-electrode array (MEA)
134 with 5'-Del, 3'-Del or control neurons co-cultured with primary mouse glial cells for six weeks to
135 promote maturation. Interestingly, spontaneous network activity (weighted mean firing rate,
136 wMFR) in *NRXN1*$^{+/-}$ iGLUT neurons was reduced by over 40% in two independent time points, at
137 weeks post induction (WPI)4 (**Fig. 2a,b** 5'-Del p = 0.0011; 3'-Del, p < 0.0001, 1-way ANOVA,
138 Dunnett's test) and WPI6 (**Fig 2c** 5'-Del p = 0.0238, 3'-Del p = 0.0211 1-way ANOVA, Dunnett's
139 test). We next examined the passive membrane properties using whole-cell patch-clamp
140 electrophysiology. The cell capacitance, membrane resistance and resting membrane potentials
141 did not significantly differ between 5'- and 3'-Del cases and control iGLUT neurons (**Fig. 2d**). To
142 examine the intrinsic excitability, we compared the input-output curve for induced firing and found
143 no statistical difference in the maximal number of evoked action potentials (**Fig. 2e**). Furthermore,
144 the voltage-dependent sodium and potassium current densities were similar between 5'-Del, 3'-
145 Del and control iGLUT neurons (**Extended Data Fig**. **3a**). Taken together, these results suggest
146 that changes in passive or intrinsic excitability membrane properties cannot explain the reduced
147 firing observed on MEAs for 5'-Del and 3'-Del in iGLUT neurons.

148 In parallel, we generated iGABA neurons with the same 5'-Del, 3'-Del, and control hiPSCs, as
149 above. We observed that immature *NRXN1*$^{+/-}$ iGABA neurons exhibited a robust ~2-fold increase
150 in population-wide wMFR activity (WPI2-3) from both 5'-Del and 3'-Del cases (5'-Del p = 0.0381,
151 3'-Del p = 0.00471-way ANOVA, Dunnett's test) (**Fig. 2f,g**). Though unexpected for GABA
152 neurons, the finding is consistent with activation of ionotropic GABA receptors leading to

153 depolarization due to little KCC2 expression and reduction of internal chloride levels[25]. Indeed,
154 immature iGABA neurons expressed higher (10-fold increase compared to WPI2 neurons) levels
155 of *SLC12A5* (the gene encoding *KCC2*) (**Extended Data Fig. 4a** $p < 0.0001$, 2-way ANOVA,
156 Dunnett's test). Furthermore, this transient hyperexcitability was pharmacologically inhibited by
157 10μM gabazine, a selective $GABA_A$ antagonist (**Extended Data Fig. 4b,c**). In mature iGABA
158 neurons (>5 weeks), post-*KCC2* switch, the average wMFR decreased in 5'-Del and 3'-Del
159 neurons (5'-Del $p = 0.0809$; 1-way ANOVA, Dunnett's test) (**Fig. 2h**). Like iGLUT neurons, the
160 passive and intrinsic excitability membrane properties of iGABA neurons were not different
161 between *NRXN1*$^{+/-}$ 5'-Del or 3'-Del and controls (**Fig. 2i,j and Extended Data Fig. 3b**).

162 Overall, these data suggest that patient-specific changes in spontaneous neural activity are not
163 driven by differences in passive and excitable membrane properties in iGLUT or iGABA neurons
164 from *NRXN1*$^{+/-}$ 5'-Del and 3'-Del patients. Furthermore, these deletions did not appear to alter
165 maturation of iGLUT or iGABA neurons, as evidenced by similar induced firing rates and resting
166 membrane potentials.

167 ***NRXN1*$^{+/-}$ 5' and 3' deletions result in divergent synaptic transmission deficits.**

168 To further dissect the factors mediating phenotypes in altered spontaneous firing, we next
169 investigated the efficacy of synaptic transmission in iGLUT and iGABA neurons. Voltage-clamp
170 recordings of spontaneous excitatory post-synaptic currents (sEPSCs, no TTX) in iGLUT neurons
171 revealed decreased frequency of events for both for 5'-Del and 3'-Del cases (**Fig. 3a**). The
172 cumulative probabilities of inter-event-intervals (IEI) for both 3'-Del ($p = 1.27E-11$, Levene's test)
173 and 5'-Del iGLUTs (5'-del $p = 2.44E-5$, Levene's test) (**Fig. 3a,b**) was significantly increased,
174 compared to controls. The sEPSC amplitude increased for 5'-Del neurons (**Fig. 3a,c**). Miniature
175 excitatory post-synaptic currents (mEPSCs, +TTX) showed similar trends in IEI but no changes
176 in amplitude sizes across genotypes (IEI 5'-del $p = 0.0411$, 1-way ANOVA, Dunnett's test)
177 (**Extended Data Fig. 5a,b**). These reductions in synaptic transmission are consistent with the
178 transcriptomic signatures; pre-synaptic (SynGO) genes showed a larger change (than post-
179 synaptic) in synaptic gene expression signatures (5'-del Pre-SynGO, $Log_2FC = 0.1252$; 3'-del Pre-
180 SynGO, $Log_2FC = -0.0156$) (**Fig. 3d,e**). We further probed transcriptional signatures of known
181 *NRXN1* trans-synaptic interaction partners that mediate synapse formation, function, plasticity
182 and are frequently linked with neuropsychiatric disease[16], and found they were represented in
183 DEGs, including *CBLN2*, *LRRTM4* and *NXPH1*, suggesting these synaptic effects are largely
184 driven by change in *NRXN1* expression (**Fig. 3f**).

185 By contrast, synaptic transmission in iGABA neurons appeared to be enhanced. The frequency
186 of spontaneous inhibitory post-synaptic currents (sIPSCs) increased, marked by a significant
187 decrease in IEI in 3'-Del iGABA neurons (3'-del p = 5.05E-5 by Levene's test) (**Fig. 3g,h)**. There
188 was no change in sIPSC amplitude (**Fig. 3g,i**). Miniature inhibitory post-synaptic currents
189 (mIPSCs) recorded in the presence of TTX and CNQX (AMPA/Kinate receptor antagonist)
190 revealed similar trends in IEI, with no change in mIPSC amplitudes (**Extended Data Fig. 5c,d**).
191 Similarly, SynGO analysis revealed concordant changes in synaptic transmission and
192 transcriptomic signatures at 3'-del Pre-SynGO (Log_2FC = 0.0324), and represented DEGs among
193 *NRXN1* trans-synaptic interaction partners *CBLN2*, *NLGN1*, *NXPH1, CASK,* and *LRRTM2-4* (**Fig.**
194 **3j-l)**.

195 Overall, patient-specific alterations in spontaneous neural activity were driven by synaptic deficits,
196 with the cell type-specific impact of aberrant *NRXN1* splicing resulting in divergent
197 neurotransmission phenotypes. Furthermore, non-recurrent LOF and GOF presented unequal
198 effect sizes between cell-types, with 5'-Del neurons being most impacted by excitatory
199 transmission, but 3'-Del neurons being affected by both excitatory and inhibitory transmission.
200 Given that deletions affected iGLUT and iGABA neurons in opposing directions, these findings
201 may implicate *NRXN1* as a key mediator of excitatory/inhibitory balance, a prevalent theme
202 among neuropsychiatric disorders[26].

203 **Region-specific organoids resolve non-autonomous defects of neurogenesis and**
204 **neuronal development.**

205 To explore the impact of aberrant *NRXN1* splicing on neural patterning[27] within a self-organized
206 microenvironment, we applied dorsal forebrain patterning to yield 5'-Del, 3'-Del and control human
207 cortical organoids (hCOs) that resemble the pallium, or applied ventral forebrain patterning to
208 generate human subpallial organoids (hSOs) that resemble the subpallium (**Fig. 4a,h**)[28,29].
209 Organoid sizes varied at early time points, but maintained consistency across genotypes by 4
210 months (**Extended Data Fig. 6a,b,g,h**). RT-qPCR validated dorsal and ventral patterning, and
211 further confirmed robust expression of mutant isoforms exclusively from the 3'-Del patients, with
212 no expression from 5'-Del and control organoids (**Extended Data Fig. 6c-e, i-k**). To unbiasedly
213 characterize transcriptomics of cortical and subpallial organoids, we performed single cell RNA-
214 seq (n = 47,460 cells from hCOs, n= 35,563 cells from hSOs using 10x genomics) at 6 months, a
215 timepoint with well characterized neural activity[28,30]. We identified subclusters of cell-types within
216 hCOs and hSOs (**Fig.4b,i**), and confirmed consistent distributions of cell clusters across

217 genotypes (**Fig. 4c,j**). Strong expression of *NRXN1* and *FOXG1* confirmed forebrain identity (and
218 excluded one of six cell lines), while *EMX1* expression confirmed dorsalization of remaining hCOs.
219 Likewise, *DLX2* expression confirmed ventralization of hSOs, with an enrichment of GABAergic-
220 fated neurons (**Fig. 4d,k and Extended Data Fig. 6f,l**).

221 A recent study demonstrated that KO of *NRXN1* increased replication of NPCs in human cells
222 and in the *xenopus* telencephalon[31]. To test if *NRXN1*$^{+/-}$ deletions could impact neurogenesis, we
223 quantified neural rosette proliferation detected with immunofluorescence by calculating the ratio
224 of *KI67* protein to *SOX2* protein expression, as markers of proliferative cells and multipotent
225 neural stem cells. In the hCO subtype (DIV55-62), 3'-Del patient rosettes exhibited increased
226 KI67:SOX2 compared to control (p = 0.0063, by 1-Way ANOVA) (**Fig. 4e,f**), while in the hSO
227 subtype, 5'- and 3'-Del rosettes had reduced *KI67:SOX2* ratios (5'-del p = 0.0004; 3'-del p =
228 0.0004, by 1-Way ANOVA) (**Fig. 4l,m**). These results may explain the variation in NPC:neuron
229 proportions across genotypes (**Fig. c,j**). Differentially expressed gene sets identified cell-type-
230 specific effects in hCO-glutamatergic, hSO-GABAergic, and astroglia clusters, with robust
231 enrichment of GO terms related to RNA splicing (from upregulated genes), and
232 neurodevelopment and synaptic function (from downregulated genes) (**Fig. 4g,n**). Much of the
233 enriched GO terms overlapped among hCO-glutamatergic and hSO-GABAergic neurons, and
234 unexpectedly certain GO terms also reached significance in hCO-astroglia, but not hSO-astroglia
235 clusters (**Extended Data Fig. 7**). Overall, these data suggest that patterns of divergent cell-type
236 specific effects, particularly at the level of neural precursor states, persisted in our 3D models of
237 forebrain development, resulting in significant changes to glutamatergic and GABAergic neurons.

238 **Isogenic validation of bidirectional excitatory-inhibitory (E-I) synaptic deficits.**

239 To further support our findings of opposing, cell-type-specific changes in glutamatergic and
240 GABAergic synaptic transmission, with unequal effect size between non-recurrent *NRXN1*
241 deletions, we utilized a more direct approach using isogenic lines to causally link aberrant splicing
242 to synaptic dysfunction and develop candidate therapies. We utilized short hairpin RNAs
243 (shRNAs) to knockdown wildtype or mutant splice isoforms to mimic LOF or rescue GOF
244 phenotypes, respectively. Targeted knockdown of constitutively expressed exon 9 (expressed in
245 all alpha isoforms but not beta isoforms) achieved mRNA knockdown of ~55% in iGLUT neurons,
246 and ~75% in iGABA neurons across two or more isogenic pairs (compared to a non-targeting
247 (NT) control shRNA) (**Extended Data Fig. 8a,e**). In iGLUT neurons, we observed decreased
248 synaptic transmission (i.e., increased sEPSC IEI, p = 2.2E-16 by Levene's Test) (**Fig. 5a,b**),

249 whereas in iGABA neurons we observed increased synaptic transmission (decreased IEI, p =
250 3.65E-8 by Levene's Test and p = 0.0092 by Student's t-test) (**Fig. 5g,h**), similar to the changes
251 with 5'-Del neurons (**Fig. 3b,h**). Transcriptomic profiles of isogenic recreation lines further
252 validated total *NRXN1* knockdown (**Extended Data Fig 7c,g)** and demonstrated DEGs related to
253 multiple aspects of synaptic function in both iGLUT (29/258 DEGs; 1.274161-fold, p = 0.1049)
254 and iGABA neurons (384/3525 genes; 1.234861-fold, p = 1.307E-6) (**Fig. 5c,l and**
255 **Supplementary Table S2**). Altogether, knockdown of wildtype splicing recapitulated cell-type-
256 specific differences in *NRXN1*$^{+/-}$ 5'-Del neurons, causally implicating decreased wildtype *NRXN1*α
257 expression (LOF) as a key driver of opposing cell-type-specific phenotypes, and displayed
258 evidence of reshaped synaptic properties.

259 For *NRXN1 3*'-Del neurons, we reasoned that reducing the expression of the GOF transcript
260 should restore the changes in synaptic transmission for both iGLUT and iGABA neurons. We
261 designed a shRNA against the mutant splice junction overlapping exons 20 and 24, expressed in
262 all 3'-Del unique *NRXN1* alpha and beta isoforms, and achieved targeted knockdown of mutant
263 splice isoforms by 95% in iGLUT, and 25% in iGABA neurons in both donors (**Extended Data Fig**
264 **6b,f**). In the donor with most robust knockdown in both iGLUT (90%) and iGABA (37%) neurons,
265 electrophysiological recordings revealed reversal of changes in synaptic transmission. In iGLUT
266 neurons, shRNA MT decreased sEPSC IEI (p < 2.2E-16 by Levene's Test and p = 0.0194) (**Fig.**
267 **5d,e**) and in iGABA neurons increased sIPSC IEI (p = 0.042 by Levene's Test) (**Fig 5j,k**), as
268 compared to shRNA-NT. Notably, the IEIs for rescued neurons appeared similar to those for
269 control iGLUT and iGABA neurons (**Fig. 3b,h**). Parallel to the LOF isogenic transcriptomic
270 profiles, the GOF isogenic line had modest changes in iGLUT neurons (3/28 DEGs; 1.214533-
271 fold, p = 0.4541 by Levene's test), but more pronounced synaptic DEGs in iGABA neurons
272 (128/1077 DEGs; 1.347225-fold, p = 2.694E-4) (**Fig. f,l and Extended Data Fig. d,h**).

273 In summary, knockdown of WT *NRXN1* in iGLUT and iGABA neurons recapitulated
274 neurotransmitter phenotypes of 5' LOF *NRXN1* deletions, while knockdown of MT isoforms
275 rescued them, appearing to mitigate the negative effect of the 3' GOF NRXN1 deletions.
276 Furthermore, the bidirectional effect of *NRXN1* deletions on iGLUTs (decrease) and iGABAs
277 (increase), i.e., E-I balance, was reversed by shRNA treatments. Transcriptomic profiling of
278 shRNA treated isogenic lines revealed ~10% of DEGs related to synaptic function across all four
279 experimental conditions. Altogether, shRNA mediated perturbations among WT and MT isoforms
280 causally implicate *NRXN1* splicing to synaptic dysfunction.

281 **Precise therapeutic targeting of stratified LOF/GOF binary phenotypes**

282 Based on our causal linkage of unique LOF/GOF aberrant *NRXN1α* splicing patterns to E-I
283 synaptic dysfunction, we stratified our patients to systematically explore novel therapeutic
284 strategies. Our findings across case/control and isogenic experiments highlight impaired E-I
285 signaling, notably a bias against excitation, via decreased glutamatergic and increased
286 GABAergic synaptic activity. As proof of principle, we tested methods to manipulate *NRXN1*
287 expression, focusing on reversing phenotypes in iGLUT neurons, to mitigate decreased
288 excitation.

289 For GOF patients, we investigated the utility of using anti-sense oligonucleotides (ASOs), which
290 have been recently used to treat different neurological diseases[32], to target a specific RNA splice
291 site. We first designed an "alternative splice matrix," by juxtaposing splice donor and acceptor
292 RNA sequences from each *NRXN1α* exon, which generates all possible combinations of
293 canonical and non-canonical splice junctions (**Fig. 6a**). We noted the sequence that covers the
294 20/24 mutant splice junction and designed an ASO to facilitate targeted RNAseH1-dependent
295 degradation of 3-Del mutant isoforms. ASO treatment (1μM) for 72hrs decreased total mutant
296 isoforms by ~55% in iGLUT neurons ($p < 0.001$ by student's t-test), as compared to a non-
297 targeting control ASO (**Fig. 6b**). Transcriptomic profiling revealed robust DEGs, enriched for
298 synaptic properties and neurotransmitter signaling and neurodevelopmental pathways
299 **(Supplementary Table S3)** (231/1844 Bonferroni corrected DEGs annotated in SynGO;
300 0.420028-fold, p = 1.016E-08), (**Fig. 6c-d**). Supporting the broader applicability of an ASO
301 strategy, we investigated the presence of mutant splice isoforms in post-mortem brain tissue from
302 an unrelated *NRXN1*$^{+/-}$ case diagnosed with autism spectrum disorder (ASD) (**Supplemental Fig.**
303 **9**). By integrating long-read and short-read sequencing[14], we identified nine high-confidence
304 isoforms that are predicted to be translated: two of which contained a novel splice junction
305 overlapping the deletion encompassing exon 14/19, targetable by an ASO tailored to mutant
306 splice junction.

307 To develop a therapeutic strategy for treating LOF patients, we took a different approach. We
308 hypothesized that enhancing transcription of the WT *NRXN1α* allele might be sufficient to restore
309 *NRXN1* levels. β-estradiol reversed *NRXN1* LOF neurogenesis deficits in *xenopus* and human
310 NPC models[31]. The mechanism is unknown, but chromatin immunoprecipitation with sequencing
311 (ChIP-Seq) in mouse brain tissue identified estrogen receptor alphaα (ERα) binding sites at the
312 *NRXN1* alpha locus (**Extended Data Fig. 10**)[33]. We predicted *NRXN1* to be a target of ERα, and

313 found that acute treatment with β-estradiol (10nM or 30nM, 3-5 days) significantly increased
314 *NRXN1α* expression in iGLUT neurons (p = 0.0297 by Student's t-test) derived from 5'-Del
315 patients (**Fig. 6f**). To test the hypothesis that chronic exposure to β-estradiol would ameliorate
316 phenotypes of iGLUT synaptic transmission, we treated post-mitotic 5'-Del neurons with either
317 30nM β-estradiol or vehicle (DMSO), and measured spontaneous neural activity with MEA and
318 synaptic transmission with patch-clamping. MEA recordings at DIV21-13 revealed a significant
319 increase in wMFR activity (p = 0.0057 via student's t-test) in the β-estradiol treated condition (**Fig.**
320 **6g**). In addition, β-estradiol treatment ameliorated the change in sEPSC IEIs in 5'-Del neurons (p
321 = 1.54E-4 by Levene's Test), but not in vehicle treated 5'-Del neurons (p = 0.9055 by Levene's
322 Test) **(Fig. 6h,i)**.

323 Altogether, increased *NRXN1* expression in LOF neurons and knockdown of mutant splicing in
324 GOF neurons can each rescue the opposing cell-type-specific case/control differences in
325 *NRXN1*$^{+/-}$ neurons, implicating *NRXN1α* expression as a key a driver of *NRXN1* mutant
326 phenotypes, and that modulators of *NRXN1* expression and splicing may be utilized for targeted
327 therapies.

328 **DISCUSSION**

329 *NRXN1*$^{+/-}$ deletions are linked to diverse clinical outcomes, all of which have been associated with
330 excitatory-inhibitory (E-I) imbalance[1,27,30]. While several studies have shed insights into the
331 regulation of synaptic properties, the molecular regulators of E-I balance has yet to be
332 characterized. Here, we show that *NRXN1* splicing bidirectionally regulates E-I synaptic
333 transmission, with the 5'-Del and 3'-Del patients reducing sEPSC but increasing sIPSC IEIs in
334 iGLUT and iGABA neurons, respectively. These changes likely play a critical role in altering the
335 E-I balance, a common theme among neuropsychiatric disorders. Using a case/control *NRXN1*$^{+/-}$
336 cohort as well as isogenic manipulations of the *NRXN1* isoform repertoire, we report distinct
337 phenotypic effects in human iGLUT and iGABA neurons, which predominately manifest in
338 changes in the frequency of synaptic transmission. These results suggest causal relationships
339 between aberrant splicing and synaptic dysfunction, dictated by unique patient-specific
340 mechanisms. A recent report evaluated the impact of *NRXN1*$^{+/-}$ on forebrain organoids by single
341 cell transcriptomic characterization over time, and highlighted specific perturbations in the
342 developmental trajectories of early neural progenitors[34]. Likewise, we report divergent
343 proliferation dynamics, with an increase in glutamatergic enriched hCOs, but a decrease in
344 GABAergic-enriched hSOs. While it is mechanistically unclear how mutations in *NRXN1* impact

345 neurogenesis, prior evidence also exists for this phenomenon[31,35], altogether suggesting roles for
346 *NRXN1* beyond mediating synaptic organization and transmission, perhaps similar to
347 *SYNGAP1*[36], a gene canonically thought to have exclusive synaptic function. Nevertheless, our
348 causal demonstration of manipulating *NRXN1* splicing, which resulted in the recreation/rescue of
349 synaptic phenotypes in post-mitotic neurons suggests that direct manipulation of splicing may
350 achieve therapeutic benefit in cases.

351 Neurexins are expressed across all synapses and among certain non-neuronal cell-types, such
352 as astrocytes, which may confer distinct functional roles[37]. With respect to GOF mechanisms, it
353 remains unclear whether mutant isoforms shift the stoichiometry of alternative splicing against
354 wildtype RNA isoforms or alter trans-synaptic protein-protein interactions. Unique patterns of
355 aberrant splicing amongst non-recurrent mutations would be challenging to target with a common
356 pharmacological agent for all *NRXN1*$^{+/-}$ carriers. Given that *NRXN1* fundamentally encodes for
357 pre-synaptic cell adhesion molecules, traditional neuropharmacological agents that target specific
358 receptors within single neurotransmission systems would be unlikely to broadly ameliorate the
359 many levels of neural circuitry impacted across neurodevelopment, especially within dysfunctional
360 synapses. Instead, precision therapies that target aberrant splicing are needed to effectively
361 reverse defects in the multiple cell types affected by patient-specific deletions.

362 Our results show that the opposing effects of *NRXN1*$^{+/-}$ in glutamate and GABA neurons provides
363 the foundation for evaluating proof-of-concept therapeutics that target aberrant splicing, once the
364 LOF or GOF phenotype has been determined. ASOs designed to target a mutant splice junction
365 to facilitate degradation of mutant isoforms represent a therapeutic approach with which to
366 ameliorate the toxic effects of GOF mutations (**Fig. 6e**). While gene therapy in brain disease has
367 resulted in mixed successes[38], cases of muscular dystrophies which have been treated via
368 splicing modulating ASOs have proved effective[39].

369 For LOF mutations, mechanisms for upregulation of wild-type allelic expression and restoration
370 of proper *NRXN1* splicing are required (**Fig. 6j**). Steroid-based pharmaceuticals for treating LOF
371 mutations is feasible, as they have been used to treat neuroinflammation-related conditions[40],
372 with recent studies revealing estrogen-mediated roles in neuroprotection[31], demonstrating the
373 safety and feasibility of this approach. Altogether, precision medicine provides therapeutic
374 promise for treating neuropsychiatric conditions.

375 Our findings with estrogen-dependent regulation of *NRXN1* expression also hint at possible

376 mechanistic explanations for the dramatic sex differences in the prevalence and severity of autism
377 spectrum disorders, for which the biological basis for the prominent male bias in diagnosis is
378 unknown[41]. At the genetic level, evidence exists for a female protective effect – the observation
379 that females have a higher threshold for reaching affectation status and require greater mutational
380 burden to express ASD phenotypes due to female-specific protective factors that lead to
381 resilience[42,43]. Estradiol ameliorates neurodevelopmental phenotypes in *xenopus* and zebrafish
382 genetic models of ASD[31,44], suggesting that estradiol might be modulating relevant circuits in the
383 setting of ASD risk genes to mitigate a range of ASD gene mutations. Estradiol modulates
384 excitatory and inhibitory circuits in the developing brain, regulating the switch from excitatory to
385 inhibitory GABAergic signaling in the hippocampus and playing a neuroprotective role against
386 glutamate-induced excitotoxicity[45,46]. Estrogens therefore may modulate neurodevelopment of
387 cells and circuits in a manner that confers resilience to ASD.

388 While our work carefully considers the cell-type specific impact of *NRXN1* splicing on non-
389 recurrent deletions by utilizing autonomous culture paradigms, it is important to acknowledge
390 certain limitations inherent in our study. Notably, the neuronal subtypes that are yielded from
391 lineage conversion can be diverse and immature, as recently characterized[47]. Furthermore, the
392 impact of *NRXN1*$^{+/-}$ on synaptic physiology across different subtypes of neurons (e.g., SST versus
393 PV expressing GABA neurons), remains to be determined. Future studies will need to
394 comprehensively assess the impact of *NRXN1*$^{+/-}$ across more discrete cell types and complex co-
395 culture systems, which may elucidate non-autonomous and activity dependent phenotypes of
396 *NRXN1*$^{+/-}$. Furthermore, it will be important to also probe the biochemical and proteomic
397 interactions of *NRXN1*. Unbiased proximity-labelling methods such as BioID[48], which may provide
398 mechanistic insights into *NRXN1* mediated synapse function, by defining alternations in binding
399 profiles from wildtype and mutant isoforms.

400 Precision medicine seeks to tailor treatments to individual patients[49]. Here we focus on the
401 possibility of stratifying cases based on inherited DNA mutations, with the goal of one day
402 providing the right therapy at the right time to the right patient. The most successful examples of
403 precision medicine to date have been in cancer[50], and monogenic disease[51], where genetic
404 analysis reveals molecular subtypes that benefit from specific treatments. In the context of brain
405 disorders, patient stratification is particularly challenging, reflecting in part the myriad rare and
406 common variants linked to disease[52]. An additional challenge, as discussed herein, is that
407 different mutations in the same genes can result in distinct phenotypic effects. Notably, genome-
408 wide disease-agnostic analyses reveal that transcription factors and nucleic acid binding proteins

409 are overwhelmingly driven by LOF mutations; whereas signaling molecules, enzymes, receptors
410 and transporters by dominant GOF mutations[53]. Therefore, a binary therapeutic approach, similar
411 to what we propose for *NRXN1*, may prove suitable for dual loss- and gain-of-function
412 mechanisms linked to mutations in other neuropsychiatric disorder-related synaptic genes (e.g.,
413 *NLGN3*[54], *CACNA1D*[55], *CACNA1C*[56], *SCN1A*[57], *SCN2A*[58]) as well as broadly in
414 neurodegenerative disease (e.g., *SOD1*[59] *TDP43*[59] *FUS/TLS*[59] *C9ORF72*[60], *AR*[61]), and many
415 short tandem repeat disorders[62]. Taken together, our work highlights important implications for
416 precision medicine, demonstrating the necessity of functionally dissecting the phenotypic impact
417 of diverse patient-specific genetic variants across cellular contexts, in order to resolve candidate
418 therapies across stratified disease mechanisms.

419 **METHODS**

420 *Plasmid designs and molecular cloning*

421 *i. TetO-Ascl1-Neo*

422 The *ASCL1* insert from TetO-Ascl1-Puro (Addgene #97329) was synthesized as a gBLOCK
423 flanked by EcoR1 cut sites, and cloned into TetO-hNgn2-Neo using EcoR1 to remove *NGN2.* The
424 recipient vector was dephosphorylated with shrimp alkaline phosphatase (rSAP NEB #M0371S)
425 during the digest, column purified and ligated at a 1:1 vector to insert ratio using the QuickLig Kit
426 (NEB #M2200S). The *ASCL1* stop codon was subsequently mutated using the QuickChange II-
427 XL site-directed mutagenesis kit (Agilent #200523) and verified via whole plasmid sequencing
428 from plasmidsaurus.

429 *ii. shRNA RNA interference constructs*

430 All shRNAs were designed and produced by Sigma-Aldrich via custom submitted sequences
431 against wildtype *NRXN1α* (constitutively expressed exon 9) and mutant *NRXN1α* (mutant 20/24
432 splice junction) cloned into TCR2 pLKO.5-puro.

433 *Cell Culture*

434 *i. hiPSC culture*

435 Passage matched (±3) human induced pluripotent stem cells (hiPSCs) were cultured in StemFlex
436 media (Life technologies #A3349401) on Matrigel (Corning, #354230). At ~70-80% hiPSCs were

437 clump passaged using 0.5mM EDTA in PBS without Mg/Ca (Life technologies #10010-031). Cells
438 were washed once and incubated for 4-7 min with EDTA at RT. The EDTA was aspirated, and
439 the remaining colonies were lifted off with 1mL of StemFlex and re-distributed at varying densities
440 in a 6–well maintenance plate. hiPSC lines were split every 4-6 days. For neuronal/organoid
441 differentiation, wells of similar confluence across all hiPSC donors were resuspended and seeded
442 onto a Matrigel coated 10cm dish and expanded until ~70-80% confluency.

443 *ii. HEK293T culture and lenti-viral production*

444 HEK293T cells were maintained in 15cm dishes and cultured in DMEM supplemented with 10%
445 standard FBS (Life technologies #16000069). 3rd Gen lenti-viral particles were produced using
446 previously described methods and REV, MDL and VSV-G plasmid ratios[18], each transfected with
447 PEImax (Polysciences #24765-1). Each PEIMax batch was volumetrically titrated at total
448 ugDNA:uLPEI for optimal transfection efficiency.

449 *iii. Primary mouse glia production*

450 All mouse work was performed under approved IACUC protocols at the Icahn School of Medicine
451 at Mount Sinai. C57BL/6 mice were used as breeding pairs. For glial preps, dissected cortices
452 from 3 pups (at p0-3) were dissociated using papain (R&D #LS003126) and plated on 10cm
453 dishes in MEF medium (DMEM, 10% Cosmic Calf Serum (Fisher #SH3008703HI), 1x Antibiotic-
454 antimycotic (Life technologies #15240), 1x Sodium Pyruvate (Life technologies #11360070), 1x
455 MEM Non-Essential Amino Acids Solution (Life technologies #11140050), 4uL 2-Mercaptoethanol
456 (Sigma #60-24-2), supplemented with 100µg/mL Normocin (InvivoGen #ant-nr-2). Glial cells were
457 recovered and propagated for 7 days, expanded into three 10cm dishes and were used for co-
458 culture experiments. All glial preps were tested twice for mycoplasma (Normocin withdrawn)
459 (Lonza, #LT07-318) prior to freezing or neuronal co-culture. At day 14, one 10cm dish with mouse
460 glia were distributed to two MEA, 12- or 24- well plates, and subsequently inactivated with 4µM
461 Ara-C (Sigma #C1768) prior to or during re-seeding of induced neurons.

462 *iv. iGLUT induction and astrocyte co-culture*

463 At day -1 hiPSCs expanded in 10cm dishes were dissociated with accutase (StemCell
464 Technologies, #07920), washed and pelleted with a 1:4 ratio of accutase to DMEM for 5 min at
465 1000 rcf, and re-suspended with StemFlex media containing ROCK inhibitor, THX (10µM/mL;
466 Sigma Aldrich, SML1045). The hiPSCs are then co-transduced with TetO-Ngn2-Puro (Addgene

467 #79049) or TetO-Ngn2-Neo (Addgene# 99378) and UCb-rtTA (legacy vector from the lab of Fred
468 Gage) and seeded at 1.0-1.5x10^6 cells in 1.5mL per well on 6-well plates were coated with 2x
469 Matrigel for at least one hour at 37C. The hiPSC-viral mixture was then incubated overnight. The
470 following morning (day 0), a full media change with iGLUT induction media was performed with
471 the following recipe: Neurobasal Media: 1x N2 (Life technologies #17502-048), 1x B-27 minus
472 Vitamin A (Life technologies #12587-010), 1x Antibiotic-Antimycotic, 1x Sodium Pyruvate, 1x
473 GlutaMax (Life technologies #35050), 500μg/mL cyclic-AMP (Sigma #D0627), 200nM L-ascorbic
474 acid (Sigma #A0278), 20ng/ml BDNF (Peprotech #450-02), 20ng/ml GDNF (Peprotech #450-10),
475 1μg/ml natural mouse laminin (Life technologies #23017015). On days 1-2, iGLUT cells were
476 treated with respective antibiotic concentrations at 1ug/mL puromycin (Sigma# P7255) or
477 0.5ug/mL neomycin (Life technologies #11811-031). On day 3, antibiotic medium was withdrawn
478 and iGLUT cells were treated with 4μM Ara-C. On Day 4, iGLUT cells were dissociated with
479 accutase for 15 min, washed and pelleted with a 1:4 ratio of accutase to DMEM for 5 min at 800
480 rcf, and re-suspended with iGLUT media containing ROCK inhibitor, Ara-C and 2% low-
481 hemoglobin FBS (R&D systems #S11510). iGLUT neurons were distributed among wells (500-
482 750k cells per 24wp or 0.75-1.5E6 cell per 12wp) pre-seeded with confluent mouse glia. The
483 following day, iGLUT neurons received a full media change with Brainphys maturation media
484 (Neurobasal Media, 1x N2, 1x B-27 minus Vitamin A, 1x Antibiotic-Antimycotic, 500μg/mL cyclic-
485 AMP, 200nM Ascorbic Acid, 20ng/ml BDNF, 20ng/ml GDNF, 2% low-hemoglobin FBS, 1μg/ml
486 Mouse Laminin) supplemented with Ara-C and were subsequently monitored for growth of non-
487 neuronal/glial cells. Ara-C treatment was tittered down with half-media changes (without Ara-C)
488 every 3-4 days until used for experiments.

489 *v. iGABA induction and astrocyte co-culture*

490 iGABA production paralleled the methods aforementioned. hiPSCs were instead co-transduced
491 with TetO-Ascl1-puro (Addgene #97330) or TetO-Ascl1-neo (Addgene #TBD), TetO-Dlx2-hygro
492 (Addgene #97329) and UCb-rtTA and seeded at 0.8-1.2x10^6 cells in 1.5mL per well on 6-well
493 plates similarly prepared. The following morning (day 0), a full media change with iGABA induction
494 media (DMEM/F-12 + Glutamax, 1x N2, 1x B-27 minus Vitamin A, 1x Antibiotic-Antimycotic) was
495 performed. On days 1-2 iGABA cells were selected with respective antibiotic concentrations at
496 1μg/mL puromycin or 0.5ug/mL neomycin and 0.25ug/mL hygromycin (Life Technologies
497 #10687010), followed by antibiotic withdrawal and Ara-C treatment on day 3. iGABA neurons
498 were re-seeded identically to iGLUT cells, at 150-250k cells per 24wp well. iGABA cultures were

499 morphologically QC'ed prior to all experiments, with uncharacteristic batches being discarded.

500 *vi. Cortical and subpallial organoid differentiation*

501 Cortical organoids were generated according to the protocol described by Sloan et. al.[63], with
502 several modifications. hiPSCs were first aggregated into embryoid bodies (EBs) using an
503 AggreWell™800 Microwell Culture Plate system (Stemcell Tech #34850). Expanded hiPSCs
504 were rinsed twice with DPBS without Ca/Mg, and then dissociated using accutase. 3x10E6
505 hiPSCs were added to a single well in the prepared AggreWell and allowed to aggregate in a 37
506 °C incubator for 24 hours. The following day (day 0), EBs were dislodged from the AggreWell
507 plate using a cut p1000 pipette tip and passed over a 40µm strainer, and washed with excess
508 DMEM. The strainer was inverted over an Ultra-Low Attachment 10 cm culture dish and the EBs
509 were collected in spheroid induction media, which contained Stemflex supplemented with two
510 SMAD inhibitors, SB-431542 (SB) and LDN193189 (LDN), and THX. The following day (day 1),
511 the media THX was withdrawn. From d2-d6, induction media was replaced daily, and no longer
512 contained the Stemflex supplement (only base Stemflex media with SB and LDN). On day 6, the
513 media was replaced with organoid patterning media, formulated with Neurobasal-A medium, 1x
514 B-27 minus Vitamin A, 1x GlutaMAX, and 1x Antibiotic-Antimycotic. From d6-d24, organoid
515 maturation media was supplemented with 20 ng/ml of EGF (R&D Systems, #236-EG) and 20
516 ng/ml FGF2 (R&D Systems, #233-FB-01M). Media was changed every day from d6 – d15, after
517 which media was changed every other day. From d25-d43, the organoid maturation media was
518 supplemented with 20 ng/ml of NT-3 (PeproTech, #450-03) and 20 ng/ml BDNF. From d43
519 onwards, organoids received organoid maturation media with no supplements, and media was
520 changed every 4 days or as needed. Subpallial organoids were generated in the same way as
521 cortical organoids, but with additions in media formulations. From d4-d23, hSOs received
522 spheroid induction media or organoid maturation media supplemented with 5 µM of the Wnt
523 inhibitor, IWP-2 (Selleckchem, #S7085). From d12-d23, hSO organoids received neuronal
524 differentiation media supplemented with 100 nM of the SHH agonist, SAG (Selleckchem,
525 #S7779).

526 <u>*Electrophysiology*</u>

527 *i. Multi-electrode array (MEA)*

528 The Axion Maestro (Middleman) system was used to perform all MEA recordings. Measurements
529 began as early as DIV9 for both iGLUT and iGABA co-cultures. For time course experiments,

530 MEA plates were recorded every 2-3 days per week with a full media change prior to each
531 recording.

532 *ii. Whole-cell patch-clamp electrophysiology*

533 For whole-cell patch-clamp recordings, iGLUT or iGABA human-mouse glia co-cultures were
534 recorded at 4-6 weeks following dox-induction (time points specified in figure legends), with a full
535 media change one day prior to recording. Cells were visualized on a Nikon inverted microscope
536 equipped with fluorescence and Hoffman optics. Neurons were recorded with an Axopatch 200B
537 amplifier (Molecular Devices), digitized at 10 kHz using a Digidata 1320a (Molecular Devices) and
538 filtered between 1-10 kHz, using Clampex 10 software (Molecular Devices). Patch pipettes were
539 pulled from borosilicate glass electrodes (Warner Instruments) to a final tip resistance of 3-5 MΩ
540 using a vertical gravity puller (Narishige). To sustain the baseline activity of neurons from
541 extended cultures, coverslips were recorded in base Brainphys medium (external solution, Osm
542 305, pH 7.49). Each coverslip was equilibrated to room temperature for 10min, with 3-5 neurons
543 were recorded for no more than a total of 75min per coverslip. For measurements of passive and
544 excitable properties, an internal patch solution was used containing (in mM): K-d-gluconate, 140;
545 NaCl, 4; MgCl2, 2; EGTA, 1.1; HEPES, 5; Na2ATP, 2; sodium creatine phosphate, 5; Na3GTP,
546 0.6, at a pH of 7.4. Osmolarity was 290-295 mOsm. Neurons were chosen at random using DIC
547 and all recordings were made at room temperature (~22°C). Current-clamp measurement
548 occurred across -10pA to +50pA steps, with a maximum stimulus of +60pA, whereas voltage-
549 clamp measurements occurred across -50mV to +50mV steps, normalized to cell capacitance (to
550 control for variable neuronal size). Current clamp measurements were corrected for the junction
551 potential (~-15.5mV). For sEPSC/sIPSC recordings, the internal solution was replaced with (in
552 mM): Cesium-Chloride, 135; HEPES-CoOH, 10; QX-314, 5; EGTA, 5. Osmolarity was 290-295
553 mOsm. All mEPSC measurements were recorded under the presence of 100nM TTX-citrate
554 (Tocris Cat# 1069). mIPSC measurements were made using 100nM TTX-citrate and CNQX-
555 disodium salt (Tocris Cat#1045/1) to pharmacologically inhibit ionotropic glutamate receptors. All
556 chemicals were purchased from Sigma-Aldrich Co. (St. Louis, MO). All toxic compounds were
557 handled in accordance with ISMMS EHS standards.

558 *iii. Patch-clamp data analysis*

559 All patch-clamp data were analyzed on Clampfit (v) and Easy-Electrophysiology (v2.4.1 or beta-
560 versions). Briefly, for voltage-clamp data, files were opened in Easy-Electrophysiology and two

561 bins were assigned for Na+/K+ measures for minimum and maximum current values, respectively.
562 For current-clamp data, files were opened in Easy-Electrophysiology and action potential (AP)
563 analysis was used to automatically determine spike number and properties. For gap-free
564 recordings, all data was post-hoc adjusted to a baseline of zero on ClampFit, and subsequently
565 analyzed in Easy-Electrophysiology by template and linear threshold detection. For case control
566 experiments, a minimum cutoff of 10 events for the duration of the recording (3min) was used as
567 QC. For typical EPSC events, a single template from a randomly chosen recording was used to
568 analyze all traces (with a 30ms decay cutoff). For IPSC events, three templates were used to
569 detect variable GABA receptor kinetics, for all traces (with a 60ms decay cutoff). An amplitude cut
570 off of 7pA was used to call positive events. For cumulative probabilities, each cell was binned by
571 experiment and averaged across all cells for a representative curve (GraphPad Prism).

572 *RNA-Sequencing and bioinformatic analyses*

573 *i. Bulk RNA sequencing and DEG analysis of iGLUT and iGABA neurons*

574 iGLUT (DIV21) and iGABA (DIV14 or DIV35) co-cultured with primary mouse glia (to match
575 functional experiments) were harvested in Trizol and submitted to the New York Genome Center
576 [64] for high-throughput RNA extraction and quality control, library prep using the Kapa Hyper library
577 prep with ribo-erase (Roche #KK8541) and subsequently sequenced on Illumina NovaSeq.
578 Returned raw data files were first processed to remove mouse reads in the RNA-seq data, a
579 combined genome reference (hg38 and mm10) was created using the "mkref" command in
580 cellranger v6.1.2. The raw sequencing reads were then aligned to the combined genome
581 reference using STAR v2.7.2a[65]. Reads that mapped specifically to the human reference genome
582 were extracted from the resulting BAM files for subsequent gene expression analysis. Gene-level
583 read counts were obtained using the Subread v2.0.1 package featureCount[66], and RPKM values
584 were calculated using the R package edgeR[67]. To confirm sample identity, variants were called
585 from RNA-seq bam files by HaplotypeCaller and GenotypeGVCFs in GATK v4.2.0.0. Then
586 bcftools v1.15 was used to examine variants concordance with variants from whole-exome
587 sequencing data from the same donor. Following donor identity confirmation, the differential gene
588 expression analysis followed the methods as described previously[68]. First, CibersortX[69] was
589 utilized to predict differences in cell type composition across all samples. The R package
590 variancePartition v1.30.2[70] was then employed to investigate the contribution of specific variables
591 to the variance in gene expression. The limma/voom package[71] was used for differential
592 expression analysis, with the regression of fibroblast and hiPSC cell type compositions. The

593 analysis began with a comparison between the case and control groups. Subsequently, within
594 each case vs control group, subgroup comparisons were conducted for all four pairs (two donors
595 each for 3'-Del and 5-Del patients and two healthy controls) of samples, accounting for
596 heterogeneity between different donors. Genes with a fold change larger than 1.5 between the
597 patient and control group, an FDR less than 0.1, and a fold change larger than 1.5 in all four pairs
598 of subgroup comparisons were defined as the final set of differentially expressed genes. Kallisto
599 v0.46.1[72] was used to calculate the *NRXN1* exon usage ratios.

600 *ii. Network Analysis of top DEGs overlapping with disease risk genes*

601 The ASD, BP, and SCZ risk gene lists were extracted from previously curated gene lists [23], Genes
602 with the top 200 smallest FDR values and a fold change larger than 1.5 in the case vs control
603 comparison were selected for the protein interaction network analysis. Then, overlapping genes
604 between the selected gene list, the disease risk gene sets, and the proteins in the SIGNOR
605 database[24] were utilized to query the SIGNOR database and build the interaction network, using
606 the "connect + add bridge proteins" search mode in The SIGNOR Cytoscape App v1.2.[73]

607 *iii. Gene ontology analysis*

608 *iv. Dissociation and 10x Single-Cell RNA sequencing of organoids*

609 Whole organoids were dissociated to the single cell level in preparation for single-cell RNA
610 sequencing using the Papain Worthington Kit (Worthington, LK003150). All solutions included in
611 the kit were prepared according to the manufacturer's instructions. 4-6 organoids were transferred
612 to one well of a low attachment 6 well plate and were washed with PBS without Ca^{2+} and Mg^{2+}.
613 Organoids were cut with a small scalpel into smaller pieces for easier dissociation. 800 µl of
614 papain solution (supplied in the kit) was added per well. Samples were incubated at 37°C for
615 about two hours or until single cell suspension was achieved. Every 15 minutes, the mixture was
616 pipetted up and down with a cut P1000 pipette tip. Once single cell suspension was reached, 500
617 µl of inhibitor solution (supplied in the kit) was added to the well. The solution was gently mixed,
618 filtered through a 70 µm-pore sieve, and transferred to a 15 ml centrifuge tube. The cells were
619 pelleted by centrifugation at 300 x g for 5 minutes at room temperature. Cell pellets were
620 resuspended in 500 µl of ice-cold 0.04% BSA diluted in PBS without Ca^{2+} and Mg^{2+}. scRNA-seq
621 was performed on 4-6 pooled 6-month-old organoids per donor line, per condition (hCS or hSS)
622 for a total of 48 organoids. A minimum of 10,000 dissociated cells were submitted for sequencing.
623 The library was prepared using the Chromium platform (10x Genomics) with the 3' gene

624 expression (3' GEX) V3/V3.1 kit. Libraries were sequenced on an Illumina NovaSeq sequencer
625 with an S4 flow cell, targeting a minimum depth of 20,000 reads per cell. The lengths for read
626 parameters Read 1, i7 index, i5 index, and Read 2 were 100, 8, 0, 100, respectively.

627 *iv. Bioinformatic analysis of scRNASeq data*

628 The raw sequencing data, represented as base call (BCL) files produced by the Illumina
629 sequencing platform, were subjected to demultiplexing and subsequent conversion into FASTQ
630 format using CellRanger software (version 6.0.0, 10x Genomics) with default parameters. The
631 software then mapped the FASTQ reads to the human reference genome (GRCh38) with default
632 parameters. Following this, the 'count' command in the Cell Ranger v6.0.0 software was utilized
633 for the quantification of gene expression. For alignment and counting, the reference genome
634 refdata-gex-GRCh38-2020-A was used, which was procured from the official 10x Genomics
635 website. We performed QC and normalization using the Seurat v3 R package[74]. For QC, we
636 filtered out low-quality cells using the following criteria: (i) cells with unique gene counts outside
637 the range of 200 to 6000; (ii) cells with more than 30% mitochondrial gene content; and [75] cells
638 with less than 2000 unique molecular identifiers[76]. Post QC, we carried out normalization, scaling
639 the gene expression measurements for each cell by the total expression, multiplied by a scale
640 factor (10,000 by default), and log-transformed the results. We extracted the expression profiles
641 of the 338 genes identified by Birrey et al[28], to reduce the dimensionality of the dataset through
642 principal component analysis (PCA), and identify statistically significant PCs using a JackStraw
643 permutation test. This was followed by non-linear dimensional reduction using the UMAP (Uniform
644 Manifold Approximation and Projection) technique for visualization. Cells were clustered based
645 on their PCA scores using the Shared Nearest Neighbor (SNN) modularity optimization-based
646 clustering algorithm in Seurat. After dimensionality reduction, we used known marker genes to
647 guide the clustering of cells. Each cluster was then annotated using cell type markers identified
648 by Birey et al[28]. Finally, we conducted differential expression analysis across the defined cell
649 clusters using the FindAllMarkers function in Seurat, which employs a Wilcoxon Rank-Sum test.
650 The significantly differentially expressed genes were then used to interpret the biological
651 significance of cell clusters. For each identified cell type, we conducted an enrichment analysis
652 using the WebGestalt (WEB-based GEne SeT AnaLysis Toolkit) online tool, with the Human
653 genome (GRCh38) as the reference set, employing a hypergeometric statistical method and the
654 Benjamini & Hochberg method for multiple test adjustment.
655

656 *v. Analysis of ChIP-sequencing data from β-estradiol treated rodent brains.*

657

658 Tracks in bigWig format were downloaded from the GEO dataset GSE144718[33]. Two peaks within
659 the *NRXN1* gene region in the mm10 genome were visualized using Spark v2.6.2[77]

660

661 *vi. Generation of long-read sequencing data from post-mortem brain tissue*

662

663 All aspects of sample processing (tissue handing, RNA extraction, library prep, QC, sequencing
664 and bioinformatic analysis) was performed as previously described (Flaherty et al).

665

666 *Therapeutic Treatments of iNeurons*

667 *i. β-estradiol treatment*

668 β-estradiol was reconstituted in DMSO and subsequently diluted in Brainphys maturation media
669 for a final concentration of 10 or 30nM. Neurons were treated for 3-5 consecutive days, with fresh
670 drug or vehicle control replenished daily (in half media changes). iGLUT and iGABA neurons were
671 treated starting from ~DIV14-18. On the final day of treatment, cells were harvested ~4 hours post
672 dosage. Chronic treatments for functional experiments extended daily β-estradiol replenishments
673 for ~14 days, and withdrawn 2-3 days prior to patch-clamp recordings.

674 *ii. Antisense Oligonucleotide treatment*

675 A single HPLC-grade ASO was designed from Qiagen (LNA GapmeR) against the mutant (Ex
676 20/24) splice junction containing a phosphorothioate modified backbone with or without a 5'-FAM
677 label for fluorescent visualization. All experiments were performed matched with a non-targeting
678 ASO as the control group. ASOs were delivered using Lipofectamine RNAiMAX Transfection
679 Reagent (Thermo, #13778075). The Lipofectamine RNAiMAX was diluted in Opti-MEM Medium
680 (Thermo, #31985070). ASO was then diluted in Opti-MEM Medium. The diluted ASO was added
681 in a 1:1 ratio to the diluted Lipofectamine RNAiMAX and incubated at room temperature for 5
682 minutes. The ASO-lipid complex was added to cells, and incubated for 72 hours post-transfection,
683 until RNA harvest.

684 *Molecular Biology and Imaging*

685 *i. RNA extraction and RT-qPCR*

686 For the isolation of RNA, 2D cells were lysed using TRIzol (Life Technologies #15596026) and
687 purified using the Qiagen miRNeasy Kit (Qiagen Cat# 74106) according to the manufacturer's
688 instructions. For 3D organoids, pooled (early timepoints) or single organoids were washed and
689 lysed using TRIzol, by manual homogenization with a pestle in a 1.5mL centrifuge tube. Following
690 purification, samples were normalized within each experiment (15-50ng) and subsequently used
691 for RT-qPCR assays using the *Power* SYBR Green RNA-to-Ct 1-Step Kit (Thermo REF 4389986).
692 Relative transcript abundance was determined using the ΔΔCT method and normalized to the
693 *ACTB* housekeeping gene. All primer sequences are listed below.

694 shRNA, primers and oligonucleotide probe sequences

Target	Sequences (5'-3')	Supplier
RT-qPCR Primer Probes		
NRXN1 (wildtype) Forward	AGAAAGATGCCAAGCACCCA	ThermoFisher
NRXN1 (wildtype) Reverse	CCCATGTCCAGGAGGAGGTA	ThermoFisher
NRXN1-20/24 (mutant) Forward	GCTACCCTGCAGCCAACC	ThermoFisher
NRXN1-20/24 (mutant) Reverse	GACCATACCCGTGGTGCTG	ThermoFisher
ACTB Forward	TGTCCCCCAACTTGAGATGT	ThermoFisher
ACTB Reverse	TGTGCACTTTTATTCAACTGGTC	ThermoFisher
MAP2 Forward	AAACTGCTCTTCCGCTCAGACACC	ThermoFisher
MAP2 Reverse	GTTCACTTGGGCAGGTCTCCACAA	ThermoFisher
NEUROD1 Forward	GGTGCCTTGCTATTCTAAGACGC	ThermoFisher
NEUROD1 Reverse	GCAAAGCGTCTGAACGAAGGAG	ThermoFisher
SLC17A7 Forward	CGCATCATGTCCACCACCAACGT	ThermoFisher
SLC17A7 Reverse	GAGTAGCCGACCACCAACAGCAG	ThermoFisher

SLC17A6 Forward	TCAACAACAGCACCATCCACCGC	ThermoFisher
SLC17A6 Reverse	GTTTCCGGGTCCCAGTTGAATTTGG	ThermoFisher
GAD65 Forward	CTATGACACTGGAGACAAGGC	ThermoFisher
GAD65 Reverse	CAAACATTTATCAACATGCGCTTC	ThermoFisher
DLX5 Forward	ACAGAGACTTCACGACTCCCAG	ThermoFisher
DLX5 Reverse	TGTGGGGCTGCTCTGGTCTA	ThermoFisher
<u>shRNA Sequences</u>		
NRXN1 wildtype mRNA (Exon 9)	ATGGAGTGGTGGCATTTAAAT	Sigma
NRXN1 mutant mRNA (Overlapping Exon 20/24)	CGCTACCCTGCAGCCAACCCA	Sigma
<u>Antisense Oligonucleotides (LNA Gapmers)</u>		
Non-targeting ASO	AACACGTCTATACGC/36-FAM/	Qiagen
NRXN1-Splice ASO	GGTTGGCTGCAGGGTA/36-FAM/	Qiagen

ii. Bright Field Imaging

For organoid perimeter analyses, brightfield microscope images of organoids were taken with a 2x objective. Image analysis was performed in ImageJ, with best fitting ovals or ellipses were selected around an organoid, and perimeter was measured.

iii. Immunostaining of 2D cultures

For immunostaining of 2D monocultures, iGLUT and iGABA neurons seeded on acid-etched coverslips coated with PEI buffered with boric acid and 4x Matrigel. Samples were washed with DPBS $Ca^{2+/}Mg2^{+}$ and fixed using cold, fresh 16% paraformaldehyde (Life Technologies, #28908), diluted to 4% for 12 minutes at RT. Coverslips were then blocked and permeabilized with 2% donkey serum in DPBS $Ca^{2+/}Mg2^{+}$ supplemented with 0.1% Triton-X (Sigma, #93443-100ML)

706 (blocking buffer), for one hour at RT. Primary antibody solutions were prepared in blocking buffer
707 and incubated overnight at 4°C. The following day, samples were washed three times with PBS,
708 and treated with secondary antibodies diluted in blocking buffer, for 1 hour in a dark chamber.
709 Finally, samples were washed three times, and stained with DAPI for 15min at RT during the final
710 wash. Coverslips were mounted with antifade (Vectashield #H-1000-10) onto glass slides and
711 stored at 4°C until imaging using an upright Zeiss LSM 780 confocal microscope.

712 *iv. Immunostaining 3D cultures*

713 For immunostaining of 3D organoids, samples were first washed with DPBS Ca^{2+}/$Mg2^{+}$ and fixed
714 using cold 4% PFA for 2 hours at 4°C. Organoids were then washed with DPBS Ca^{2+}/$Mg2^{+}$
715 supplemented with 10% sucrose (Sigma, #S0389-500G) for one hour. Sucrose percent was
716 increased to 20% for an additional hour, and finally 30% for an overnight incubation. The following
717 day, upon observing the organoids saturated sunk to the bottom of the 1.5mL tube, organoids
718 were transferred to OCT (Sakura #4583) twice in order to remove residual sucrose solution, and
719 snap frozen in a cryopreservation mold with dry ice and stored at –80°C until cryosectioned.
720 Organoids were sectioned at 20 µm thickness onto a Superfrost *Plus* slide (Fisher Scientific, #22-
721 037-246) and stored at -20°C until immunohistochemistry staining. Boundaries were drawn
722 around tissue sections with a lipid pen (Fisher Scientific, #NC9545623) to contain solution and
723 slides were washed once with DPBS with Ca^{2+}/Mg^{2+} to remove excess OCT compound. Slides
724 were then washed twice with 0.01% Triton-X in DPBS with Ca^{2+}/Mg^{2+} (DPBS-TX) and were
725 blocked in 2% Donkey Serum in DPBS-TX for one hour at RT. Primary antibody incubation
726 mixtures were diluted in 2% Donkey Serum in DPBS-TX (see below for a list of primary and
727 secondary antibodies and dilutions used). 100 µl of primary antibody mixtures was added per
728 slide, and allowed to incubate overnight in a humidified chamber at 4°C. Pieces of parafilm were
729 added on top of primary antibody mixtures to further prevent dehydration of slides. The following
730 day, slides were washed three times with DPBS-TX. Secondary antibodies were diluted in DPBS-
731 TX and were allowed to incubate for an hour. Slides were again washed three times with DPBS-
732 TX. A 1:2000 DAPI solution diluted in DPBS-TX was applied to slides for 10 minutes. Secondary
733 and DAPI stainings took place in a covered chamber in order to minimize exposure to light. Slides
734 were washed twice with DPBS-TX, and then once with DPBS with Ca^{2+} and Mg^{2+}. Slides were
735 mounted with coverslips using Aqua Polymount solution (Polysciences #18606-20). Slides were
736 stored at -20 °C until they were imaged.

Target	Antibody Dilution	Supplier/ CAT#
Primary Antibodies		
MAP2AB	1:500	Sigma, #M1406
(Rabbit) vGAT	1:500	Synaptic Systems, #135-303
(Rabbit) vGLUT1	1:500	Synaptic Systems, #131-002
SOX2	1:200	Santa Cruz Biotechnology, #sc-365964
(Rabbit) KI67	1:300	Abcam, #ab15580
(Chicken) MAP2	1:250	Aves Labs, #MAP
DAPI	1:1000	Sigma, #D9542
Secondary Antibodies		
(Donkey) 488-Mouse	1:200	Jackson ImmunoResearch, # 711-545-152
(Donkey) 568-Rabbit	1:200	Abcam, #ab175700
(Donkey) 647-Chicken	1:200	Jackson ImmunoResearch, # 703-605-155
(Donkey) 568-Mouse	1:500	Invitrogen (A10037)
(Donkey) 488-Rabbit	1:1000	Life Technologies (A-21206)

Statistics

No statistical power estimation analyses were used to predetermine sample sizes, where were chosen to match previous publications[14,21] and field standards. All experimental statistics were performed in Prism *v10.1.1* and R *v4.2.0.* Bioinformatic analyses were performed in R *v3.5.3* (Bulk RNASeq DEG), *v4.1.2* (Bulk RNASeq GO) and *v4.1.2* (scRNAseq).

Data and Code Availability

All source donor hiPSCs have been deposited at the Rutgers University Cell and DNA Repository (study 160; http://www.nimhstemcells.org/) and all bulk and single-cell transcriptome sequencing

data are being prepared for deposits to GEO. To facilitate improved reproducibility of our data analyses, custom scripts will be deposited to github post peer-review.

Acknowledgements

MBF is supported by a Gilliam Fellowship from the Howard Hughes Medical Institute. This work is supported by the National Institute of Mental Health grants RO1 MH121074-02 (KJB, GF and PAS) and RO1 MH125579-02 (GF and KJB). We thank the Stem Cell Engineering Core at the Icahn School of Medicine at Mount Sinai. The authors are grateful to the labs of Nan Yang (Ruiqi Hu and Xiaoting Zhou) and Samuele Marro (Madel Durens) for assistance in primary glial preparations. The authors thank Kayla G. Townsley and Mark G. Baxter for advice on statistical testing. We acknowledge Daniel Weinberger and the Lieber Institute for Brain Development at Johns Hopkins School of Medicine, for sharing post-mortem materials. Finally, the authors thank all members of the Brennand, Slesinger and Fang labs for critical feedback and discussions throughout the course of this work.

Author Information

MBF, SK, ANM, RO, CP, AP performed and analyzed experiments supervised by PAS and KJB. YZ and YF performed bioinformatic analyses supervised by GF. SG contributed to RNASeq analyses. SW produced virus for the generation of iGABA neurons. EKF processed post-mortem tissue and generated long-read data. IKP assisted in statistical analyses. MBF, GF, PAS and KJB wrote the paper with input from all authors.

Ethics declarations / Competing interest statement.

All authors have no competing interests to declare.

Figures

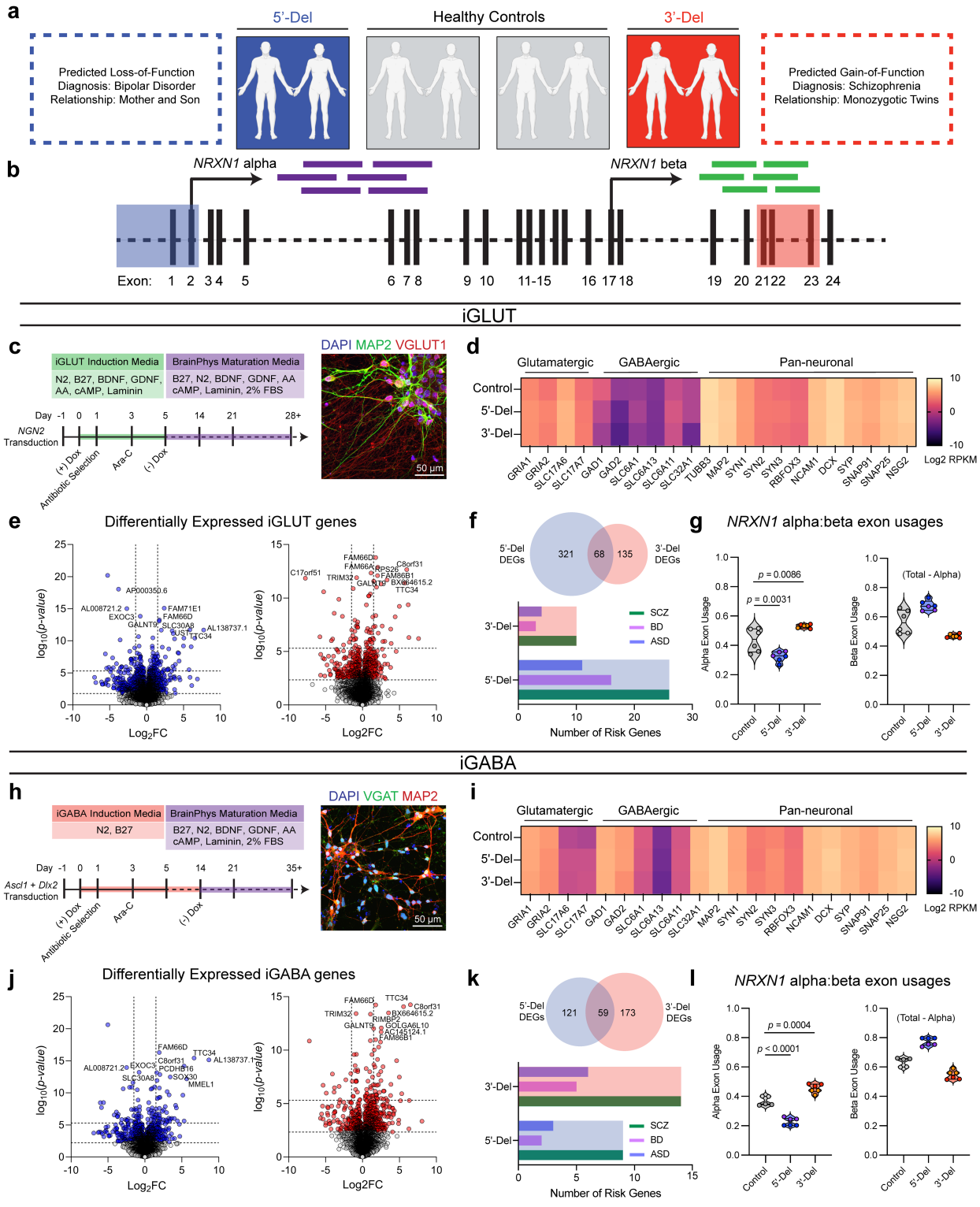

Figure 1. *Changes in NRXN1 splicing are conserved across human iPSC derived glutamatergic (iGLUT) and GABAergic (iGABA) neurons.* (**a**) Brief description of clinical information of all hiPSC

771 lines used in this study, and (**b**) schematic of *NRXN1* gene structure with red and blue shades
772 corresponding on 3'-Del and 5'-Del genotypes, respectively. Arrows indicate relative internal
773 promoter positions with purple bars corresponding to alpha exons, and green bars correlating to
774 beta exons. (**c, h**) Induction timeline and factors to generate iGLUT and iGABA neurons, with
775 immunostaining validation of neuronal identity (MAP2), glutamate identity (vGLUT1), and GABA
776 identity (vGAT). (**d, i**). Gene expression panel confirming abundance of neuronal markers and
777 neurotransmitter identity in iGLUT (n: Control = 6/2; 5'-Del = 6/2; 3'-Del = 6/2 | 1 batch) and in
778 iGABA neurons (n/d: Control = 5/2; 5'-Del = 6/2; 3'-Del = 6/2 | 1 batch). (**e, j**) Volcano plots of
779 differential gene expression (DE) analysis across both genotypes in iGLUT and iGABA neurons.
780 Vertical dashed lines represent DE genes above/below 1.5 Log_2FC. Horizontal dashed lines
781 represent FDR = 0.1 cutoff (lower) and Bonferroni corrected cutoff (upper). (**f, k**) Overlap of DEGs
782 between genotypes and enrichment of genes across neuropsychiatric disorders. (**g, l**) Percent
783 usage of alpha *NRXN1* exon usage in iGLUT, compared via a 1-way ANOVA, with Dunnett's test
784 ($F_{2, 15} = 25.70$; 5'-Del $p = 0.0031$, 3'-Del $p = 0.0086$), and iGABA neurons ($F_{2, 14} = 92.92$; 5'-Del p
785 < 0.001, 3'-Del $p = 0.0004$), with beta *NRXN1* exon usage, calculated by subtracting alpha-
786 specific reads against total reads. Data represented as mean ± sem. n reported as n (samples)/d
787 (donors) | independent batches.

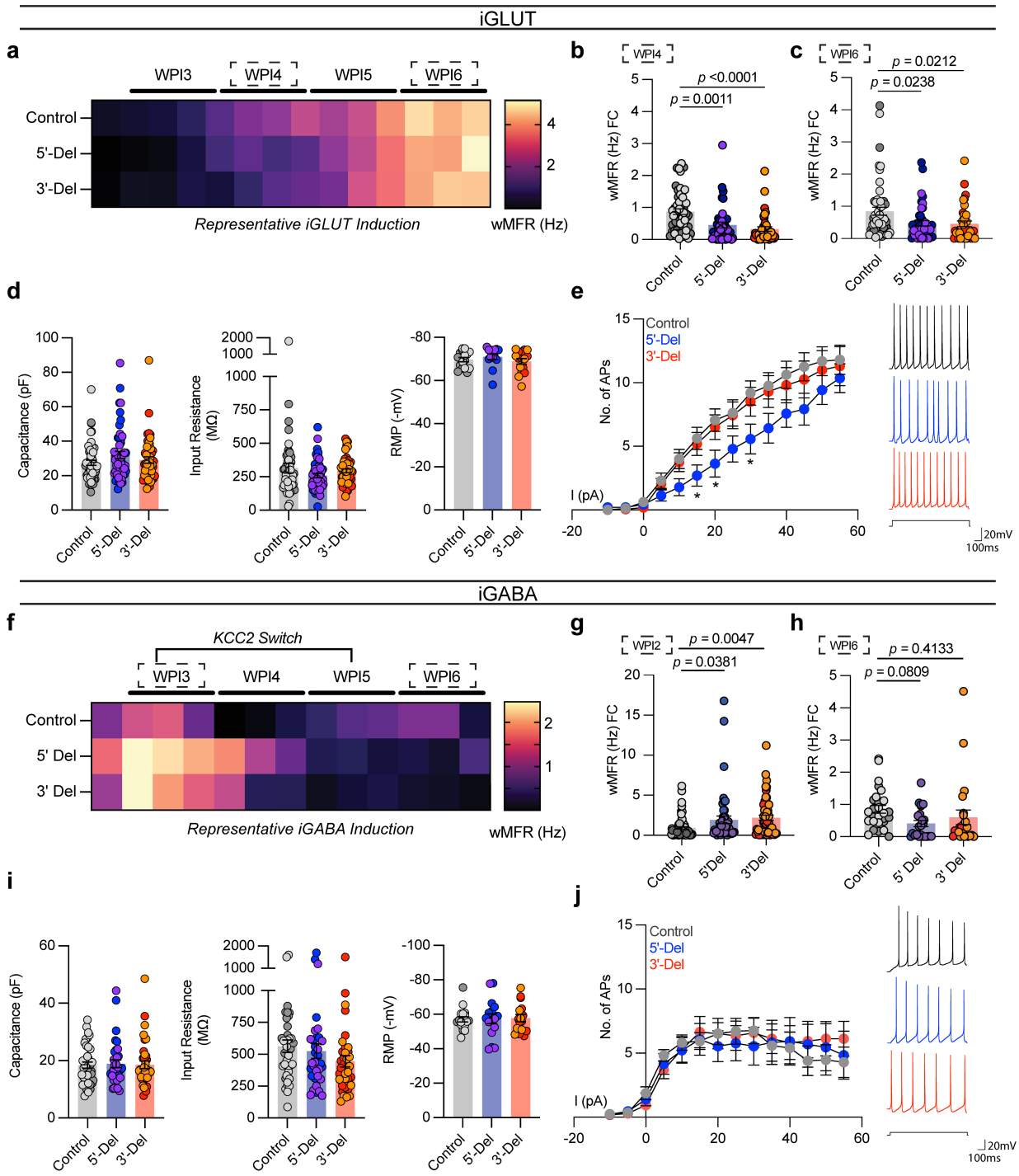

Figure 2. *Spontaneous, passive, and excitable properties are minimally changed from NRXN1$^{+/-}$ induced neurons.* (**a, f**) Timelapse of multi-electrode array recordings every 2-3 days apart starting near ~DIV12 for a single representative induction. Tiles represent averaged wMFR values across genotypes during a single recording session. (**b**) MEA quantification of iGLUT neuronal activity

(n/d: Control = 52/2; 5'-Del = 42/2; 3'-Del = 38/2 | 3 batches) at WPI4 ($F_{2, 129}$ = 11.64; 5'-Del p = 0.0001, 3'-Del p = 0.0011), and (**c**) WPI6 ($F_{2, 129}$ = 4.560; 5'-Del p = 0.0238, 3'-Del p = 0.0211). (**d**) intrinsic properties of iGLUT neurons (n/d: Control = 51/2; 5'-Del = 51/2; 3'-Del = 48/2 | 8 batches): compared via 1-way ANOVA, with Dunnett's test, Capacitance ($F_{2, 147}$ = 1.505; 5'-Del p = 0.1565, 3'-Del p = 0.7633), Input resistance ($F_{2, 147}$ = 1.311; 5'-Del p = 0.1949, 3'-Del p = 0.7906), and RMP (n/d: Control = 16/2; 5'-Del = 14/2; 3'-Del = 16/2 | 2 batches) compared via 1-way ANOVA, with Dunnett's test ($F_{2, 43}$ = 0.8234; 5'-Del p = 0.6378, 3'-Del p = 0.8468). (**e**) Input-output curves of excitable properties (n/d: Control = 16/2; 5'-Del = 14/2; 3'-Del = 16/2 | 2 batches), with representative traces (right), compared via Step x Genotype 2-way ANOVA; Dunnett's Test ($F_{26, 559}$ = 1.690, 5'-Del p < 0.01 at Step 6, 7 and 9, 3'-Del p = n.s. on all steps). (**g**) MEA quantification of iGABA neuronal activity at WPI2 (n/d: Control = 71/2; 5'-Del = 48/2; 3'-Del = 55/2 | 5 batches) compared via 1-way ANOVA, with Dunnett's test ($F_{2, 171}$ = 5.422; 5'-Del p = 0.0381, 3'-Del p = 0.0047), and (**h**) WPI5 (n/d: Control = 27/4; 5'-Del = 23/2; 3'-Del = 23/2 | 2 batches) compared via 1-way ANOVA, with Dunnett's test ($F_{2, 70}$ = 2.132; 5'-Del p = 0.0809, 3'-Del p = 0.4134). (**i**) intrinsic properties of iGABA neurons (n/d: Control = 39/2; 5'-Del = 34/2; 3'-Del = 37/2 | 6 batches): compared via 1-way ANOVA, with Dunnett's test, Capacitance ($F_{2, 107}$ = 0.04256; 5'-Del p = 0.9425, 3'-Del p = 0.9941), Input resistance (n/d: Control = 39/2; 5'-Del = 34/2; 3'-Del = 36/2 | 6 batches, $F_{2, 106}$ = 1.451; 5'-Del p = 0.8162, 3'-Del p = 0.1703) and RMP (n/d: Control = 18/2; 5'-Del = 16/2; 3'-Del = 16/2 | 2 batches) compared via 1-way ANOVA, with Dunnett's test ($F_{2, 47}$ = 0.02842; 5'-Del p = 0.9893, 3'-Del p = 0.9601). (**j**) Input-output curves of excitable properties (n/d: Control = 16/2; 5'-Del = 14/2; 3'-Del = 16/2 | 2 batches), with representative traces (right), compared via Step x Genotype 2-way ANOVA; Dunnett's Test ($F_{26, 572}$ = 0.5137, 5'-Del and 3'-Del p = n.s. on all steps). Data represented as mean ± sem. n reported as n (samples)/d (donors) | independent batches.

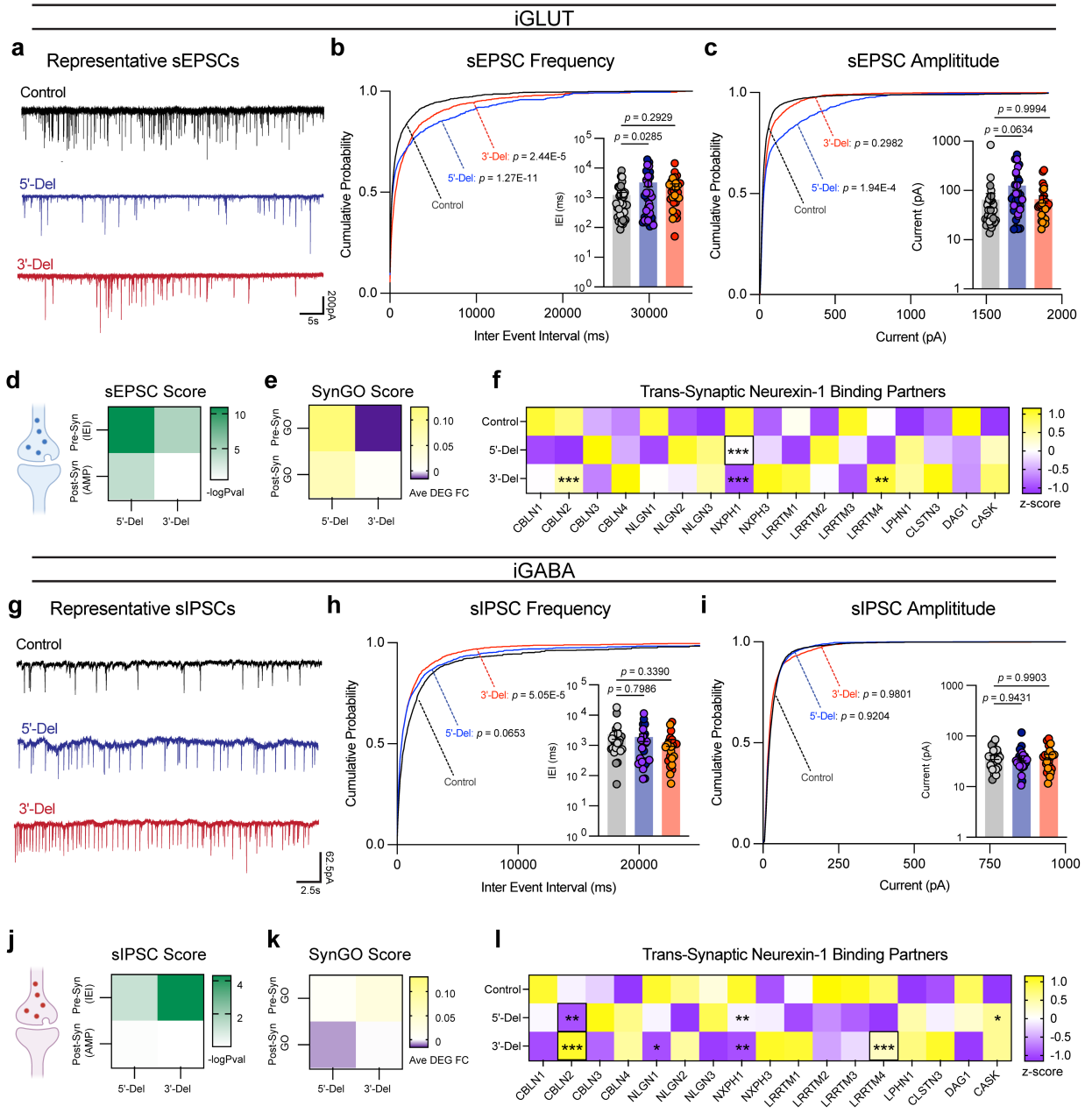

Figure 3: *Divergent impact on neurotransmission from NRXN1$^{+/-}$ induced neurons.* (**a**) Representative traces of iGLUT sEPSCs. (**b**) Cumulative probabilities and log-scaled cell averages of inter-event-internals (IEIs) across genotypes (n/d: Control = 39/4; 5'-Del = 33/3; 3'-Del = 29/2 | 6), compared by Levene's Test for averaged distributions (5'-Del F = 46.635, df = 1, p = 1.27E-11; 3'-Del F = 17.928, df = 1, p = 2.44E-5), and 1-way ANOVA, with Dunnett's test for inset ($F_{2, 98}$ = 3.117; 5'-Del p = 0.0285, 3'-Del p = 0.2929). (**c**) Cumulative probabilities and log-scaled cell averages of amplitude size across genotypes, compared by Levene's Test for averaged distributions (5'-Del F = 14.15, df = 1, p = 1.94E-4; 3'-Del F = 1.0851, df = 1, p = 0.2982),

826 and 1-way ANOVA, with Dunnett's test for inset ($F_{2, 98}$ = 2.839; 5'-Del p = 0.0634, 3'-Del p =
827 0.9994). (**d**) Transformed p-values of Levene's Test and (**e**) SynGO gene-set averaged log_2FC
828 values across pre- or post- synaptic genes. (**f**) Gene expression panel (z-scores), of canonical
829 *NRXN1* binding partners in iGLUT neurons, boxes indicate reaching genome wide significance.
830 (**g**) Representative traces of iGABA sIPSCs. (**h**) Cumulative probabilities and log-scaled cell
831 averages of inter-event-internals (IEIs) across genotypes (n/d: Control = 26/2; 5'-Del = 25/3; 3'-
832 Del = 22/2 | 4), compared by Levene's Test for averaged distributions (5'-Del F = 3.4002, df = 1,
833 p = 0.0653; 3'-Del F = 16.501, df = 1, p = 5.00E-05), and 1-way ANOVA, with Dunnett's test for
834 inset ($F_{2, 70}$ = 0.7986; 5'-Del p = 0.7986, 3'-Del p = 0.339). (**i**) Cumulative probabilities and log-
835 scaled cell averages of amplitude size across genotypes, compared by Levene's Test for
836 averaged distributions (5'-Del F = 0.1, df = 1, p = 0.9204; 3'-Del F = 0.0006, df = 1, p = 0.9801),
837 and 1-way ANOVA, with Dunnett's test for inset ($F_{2, 70}$ = 0.08143; 5'-Del p = 0.9431, 3'-Del p =
838 0.9904). (**j**) Transformed p-values of Levene's Test and (**k**) SynGO gene-set averaged log_2FC
839 values across pre- or post- synaptic genes. (**l**) Gene expression panel (z-scores), of canonical
840 *NRXN1* binding partners in iGABA neurons, boxes indicate reaching genome wide significance.
841 *p < 0.05, **p < 0.01, ***p <0.001, Wilcoxon's rank sum test, FDR = 0.05. Data represented as
842 mean ± sem. n (samples)/d (donors) | independent batches.

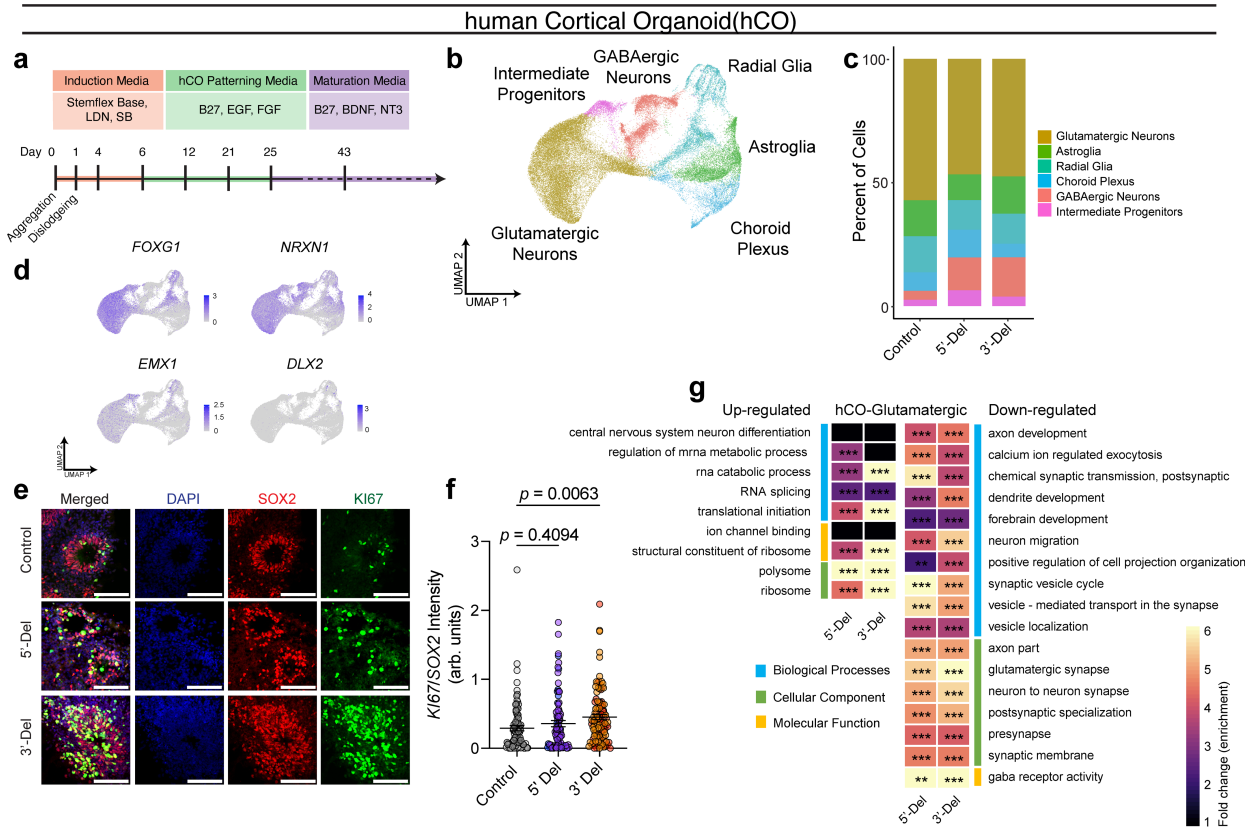
human Cortical Organoid(hCO)
a
Induction Media
Stemflex Base, LDN, SB
hCO Patterning Media
B27, EGF, FGF
Maturation Media
B27, BDNF, NT3
Day 0 1 4 6 12 21 25 43
Aggregation
Dislodgeing
b
Intermediate Progenitors
GABAergic Neurons
Radial Glia
Astroglia
Glutamatergic Neurons
Choroid Plexus
UMAP 2
UMAP 1
c
Percent of Cells
Control
5'-Del
3'-Del
Glutamatergic Neurons
Astroglia
Radial Glia
Choroid Plexus
GABAergic Neurons
Intermediate Progenitors
d
FOXG1
NRXN1
EMX1
DLX2
e
Merged
DAPI
SOX2
KI67
Control
5'-Del
3'-Del
f
p = 0.0063
p = 0.4094
KI67/SOX2 Intensity (arb. units)
Control
5' Del
3' Del
g
Up-regulated
hCO-Glutamatergic
Down-regulated
central nervous system neuron differentiation
regulation of mrna metabolic process
rna catabolic process
RNA splicing
translational initiation
ion channel binding
structural constituent of ribosome
polysome
ribosome
axon development
calcium ion regulated exocytosis
chemical synaptic transmission, postsynaptic
dendrite development
forebrain development
neuron migration
positive regulation of cell projection organization
synaptic vesicle cycle
vesicle - mediated transport in the synapse
vesicle localization
axon part
glutamatergic synapse
neuron to neuron synapse
postsynaptic specialization
presynapse
synaptic membrane
gaba receptor activity
5'-Del
3'-Del
Biological Processes
Cellular Component
Molecular Function
Fold change (enrichment)

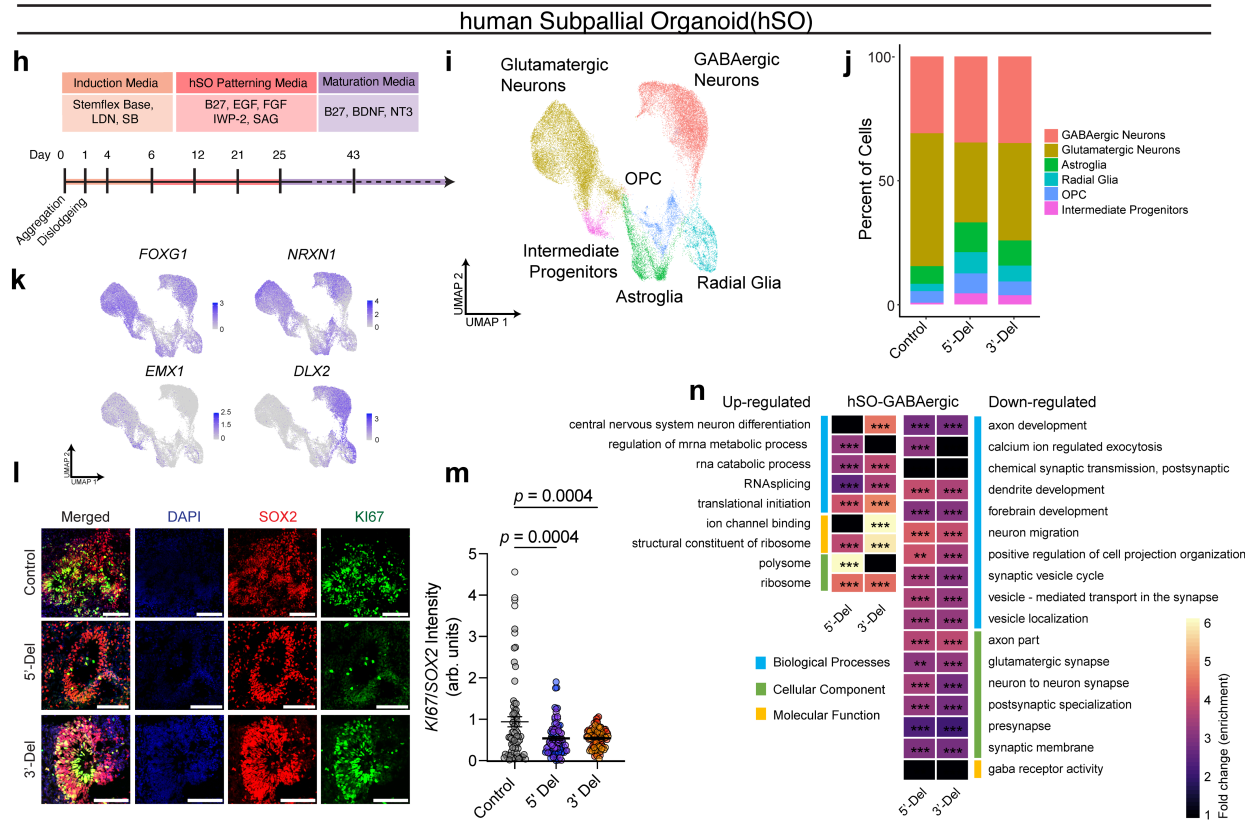
human Subpallial Organoid(hSO)
h
Induction Media
Stemflex Base, LDN, SB
hSO Patterning Media
B27, EGF, FGF IWP-2, SAG
Maturation Media
B27, BDNF, NT3
Day 0 1 4 6 12 21 25 43
Aggregation
Dislodgeing
i
Glutamatergic Neurons
GABAergic Neurons
OPC
Intermediate Progenitors
Astroglia
Radial Glia
UMAP 2
UMAP 1
j
Percent of Cells
Control
5'-Del
3'-Del
GABAergic Neurons
Glutamatergic Neurons
Astroglia
Radial Glia
OPC
Intermediate Progenitors
k
FOXG1
NRXN1
EMX1
DLX2
l
Merged
DAPI
SOX2
KI67
Control
5'-Del
3'-Del
m
p = 0.0004
p = 0.0004
KI67/SOX2 Intensity (arb. units)
Control
5' Del
3' Del
n
Up-regulated
hSO-GABAergic
Down-regulated
central nervous system neuron differentiation
regulation of mrna metabolic process
rna catabolic process
RNAsplicing
translational initiation
ion channel binding
structural constituent of ribosome
polysome
ribosome
axon development
calcium ion regulated exocytosis
chemical synaptic transmission, postsynaptic
dendrite development
forebrain development
neuron migration
positive regulation of cell projection organization
synaptic vesicle cycle
vesicle - mediated transport in the synapse
vesicle localization
axon part
glutamatergic synapse
neuron to neuron synapse
postsynaptic specialization
presynapse
synaptic membrane
gaba receptor activity
5'-Del
3'-Del
Biological Processes
Cellular Component
Molecular Function
Fold change (enrichment)

844 **Figure 4:** *NRXN1$^{+/-}$ impacts patterning of region-specific human brain organogenesis.* (**a, h**)
845 Timeline of organogenesis protocols (**b, i**), UMAPs of hCO and hSO organoid samples sequenced
846 at 6 months, annotated by cell clusters, and (**c, j**) relative proportions of cell clusters across
847 genotypes, (hCO = 47,460 cells) and (hSO = 35,563 cells). (**d, k**) validation of regionalization
848 across forebrain (*FOXG1*), dorsal (*EMX1*) and ventral (*DLX2*) regions, with *NRXN1* expression
849 across all cells. (**e, l**) Representative images of neural rosettes, immunostained with SOX2, KI67
850 and DAPI, across genotypes with (**f, m**) quantified intensity ratios for hCO (n/d: Control = 92/2; 5'-
851 Del = 84/3; 3'-Del = 108/2 | across 3-4 organoids per group from 2 batches), compared via 1-way
852 ANOVA, with Dunnett's test ($F_{2, 281} = 4.490$; 5'-Del $p = 0.4094$, 3'-Del $p = 0.0063$), and (n/d: Control
853 = 73/2; 5'-Del = 79/3; 3'-Del = 79/2| across 3-4 organoids per from 2 batches), compared via 1-
854 way ANOVA, with Dunnett's test ($F_{2, 228} = 9.366$; 5'-Del $p = 0.0004$, 3'-Del $p = 0.0004$). (g, n) Gene
855 ontological analysis results using DEGs from scRNASeq. $^{*}P < 0.05$, $^{**}P < 0.01$, $^{***}P < 0.001$,
856 Wilcoxon's rank sum test, FDR = 0.05. Data represented as mean ± sem. n reported as n
857 (samples)/d (donors) | independent batches.

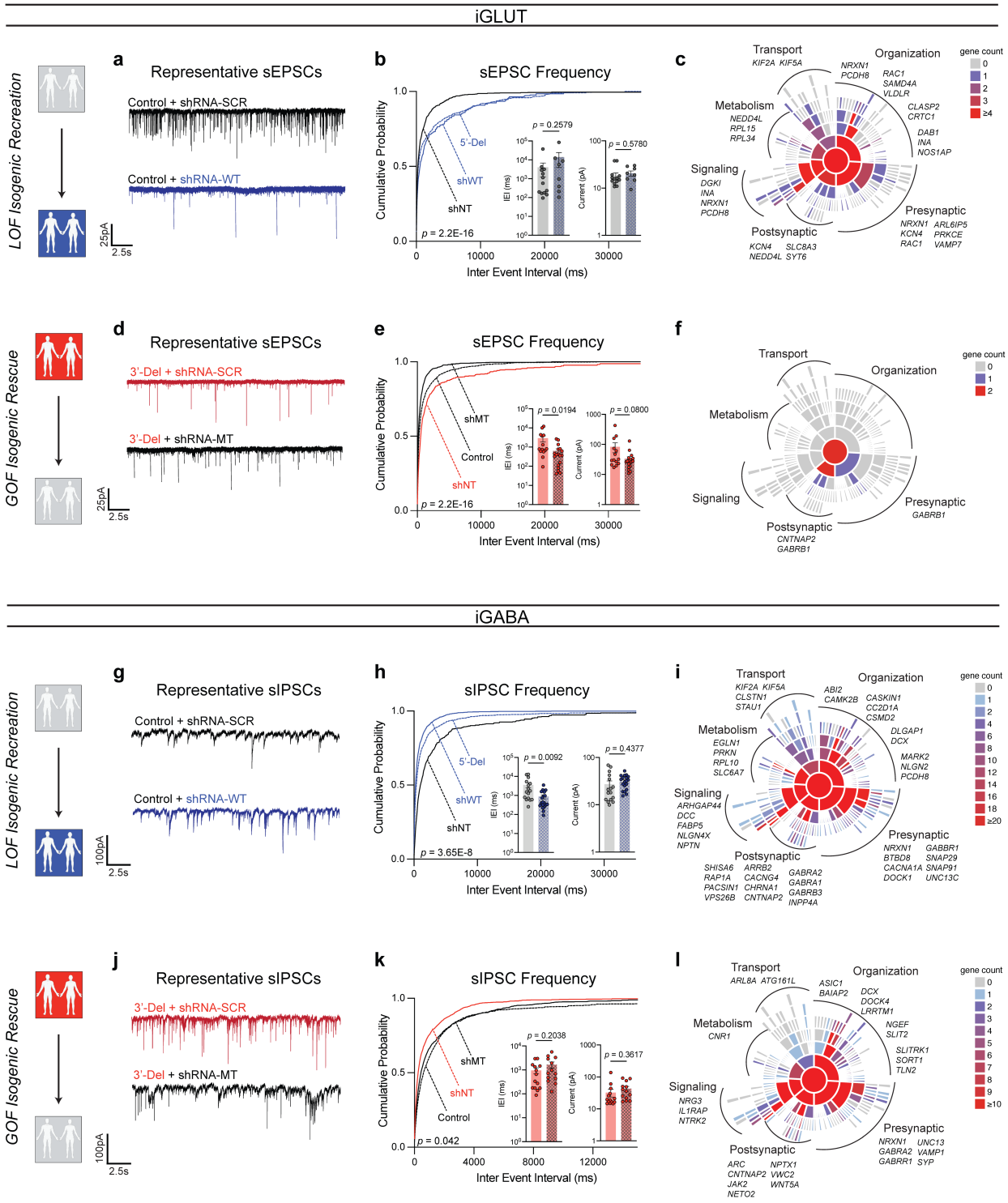

Figure 5: *Isogenic recapitulation and rescue of neurotransmission phenotypes.* (**a**) Representative traces of iGLUT WT knockdown effects, with (**b**) cumulative probabilities of sEPSC IEI distributions, with insets of cell-averaged IEI and amplitude measures (n/d: shNT = 12/1; shWT = 7/1 | 2 batches). Curves were compared via a Levene's test (F = 70.78, df =1, p <

863 2.2E-16), and insets were compared via a Student's t-test (IEI t=1.166, df=19, p = 0.2579; AMP
864 t=0.5661, df=19, p = 0.578). (**c**) SynGO (biological process) sunburst plots showing enrichment
865 of DEGs associated with synaptic function for iGLUT WT-KD compared to a brain expressed
866 background via Fisher's exact test (Fold =1.274161, p = 0.1049). (**d**) Representative traces of
867 iGLUT MT knockdown effects, with (**e**) cumulative probabilities of sEPSC IEI distributions, with
868 insets of cell-averaged IEI and amplitude measures (n/d: shNT = 14/1; shMT = 18/1 | 2 batches).
869 Curves were compared via a Levene's test (F = 230.6; df = 1, p < 2.2E-16), and insets were
870 compared via a Student's t-test (IEI t=2.471, df=30, p = 0.0194; AMP t=1.812, df=30, p = 0.08).
871 (**f**) SynGO (biological process) sunburst plots showing enrichment of DEGs associated with
872 synaptic function for iGLUT MT-KD compared to a brain expressed background via Fisher's exact
873 test (Fold = 1.214533, p = 0.4541). (**g**) Representative traces of iGABA WT knockdown effects,
874 with (**h**) cumulative probabilities of sIPSC IEI distributions, with insets of cell-averaged, IEI and
875 amplitude measures (n/d: shNT = 16/3; shWT = 19/3 | 2 batches). Curves were compared via a
876 Levene's test (F = 30.879, df =1, p < 3.66E-08), and insets were compared via a Student's t-test
877 (IEI t=2.768, df=33, p = 0.0092; AMP t=0.7856, df=33, p = 0.4377). (**i**) SynGO (biological process)
878 sunburst plots for iGABA WT-KD compared to a brain expressed background via Fisher's exact
879 test (Fold = 1.234861, p = 1.347E-06). (**j**) Representative traces of iGABA MT knockdown effects,
880 with (**k**) cumulative probabilities of sIPSC IEI distributions, with insets of cell-averaged, IEI and
881 amplitude measures (n/d: shNT = 16/1; shMT = 19/1 | 2 batches). Curves were compared via a
882 Levene's test (F = 4.1324; df = 1, p < 0.04226), and insets were compared via a Student's t-test
883 (IEI t=1.305, df=25, p = 0.2038; AMP t=0.9292, df=25, p = 0.3617). (**l**) SynGO (biological process)
884 sunburst plots for iGABA WT-KD compared to a brain expressed background via Fisher's exact
885 test (Fold = 1.347225, p = 2.694E-04). Data represented as mean ± sem. n reported as n
886 (samples)/d (donors) | independent batches.

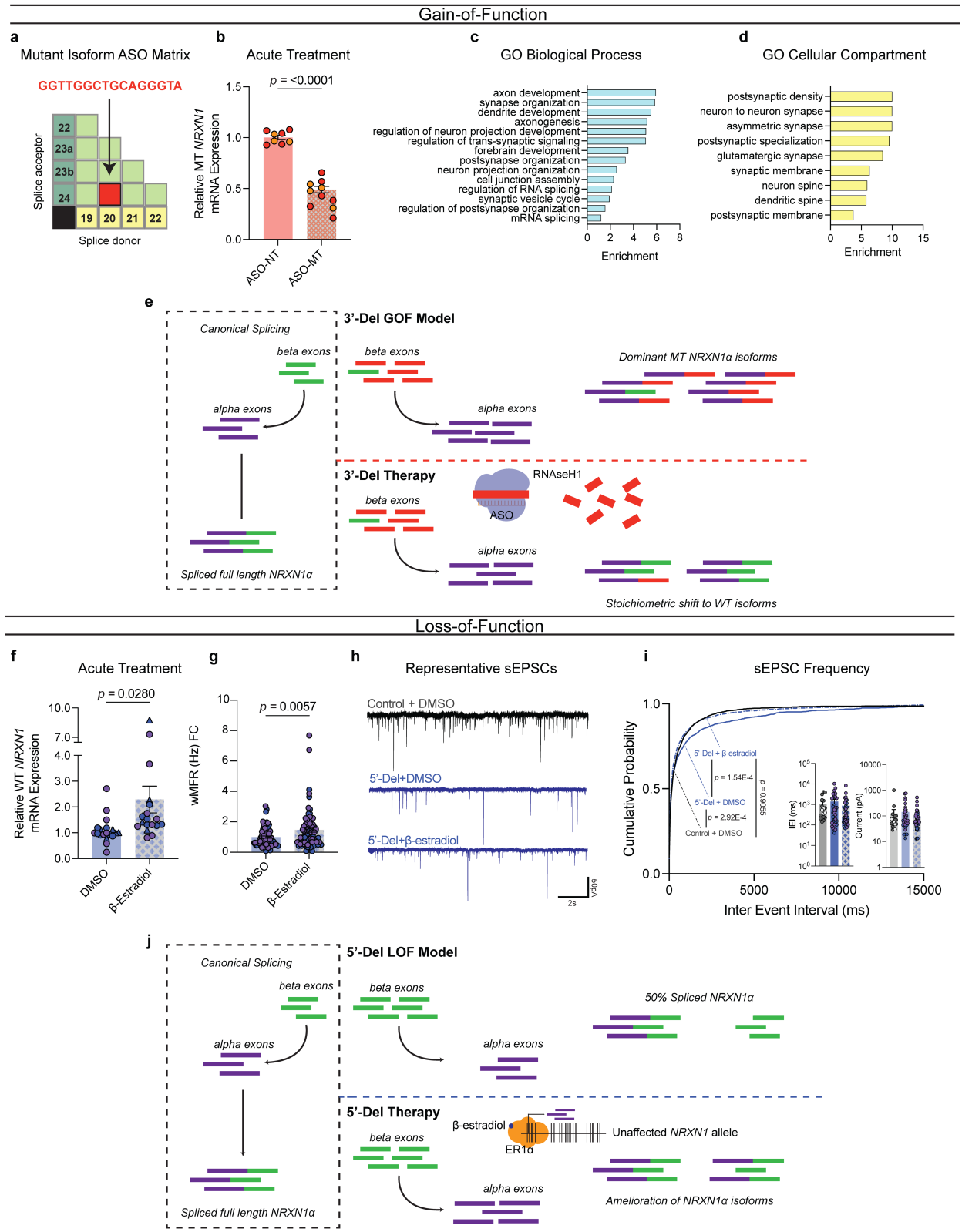

887

888 **Figure 6:** *Precise therapeutic targeting of GOF- and LOF-NRXN1$^{+/-}$ in iGLUT neurons.* (**a**)

Schematic of a *NRXN1* ASO matrix, with the selective sequence targeting 20/24 splice junction. (**b**) RT-qPCR of MT *NRXN1* gene expression in 3'-Del patients' post-acute treatment for 72hrs (n/d: ASO-NT = 8/2; ASO-MT = 10/2 | batches),compared via Student's t-test t=12.91, df=16 $p < 0.0001$. (**c**) RNASeq analysis on ASO treated patients (n/d: ASO-NT = 4/2; ASO-MT = 4/2 | representative batch), demonstrating biological process and (**d**) cellular compartment GO terms demonstrating enrichment ($\log_{10}$[adj *p* value]) of selected synapse related pathways. (**e**) Model and proposed mechanism of rescue for GOF patients expressing mutant isoforms. (**f**) RT-qPCR of WT *NRXN1* gene expression in 5-Del patients, post-acute treatment (3-5 days) (n/d: DMSO = 19/2; β-estradiol = 18/2 | 3 batches) compared via Student's t-test t=2.293, df=35$p = 0.028$. (**g**) Quantification of iGLUT neuronal activity at WPI3 across vehicle and treatment (n/d: DMSO = 72/3; β-estradiol = 74/3 | 3 batches)) compared via Student's t-test (t=2.804, df=144, $p = 0.0057$). (**h**) Representative patch-clamp traces and (**i**) cumulative probabilities of sEPSC IEI distributions, with insets of cell-averaged, IEI and amplitude measures (n/d: Control + DMSO = 18/1; 5'-Del + DMSO = 33/2 5'-Del + β-estradiol = 35/2). Curves were compared via Levene's test (Control + DMSO v 5'-Del + DMSO F = 13.151; df = 1, $p = 2.921E-4$; 5'-Del + DMSO v 5'-Del + β-estradiol F = 14.359; df = 1, $p = 1.54E-04$; Control + DMSO v 5'-Del + β-estradiol, F = 0.0141; df = 1, $p = 0.955$). Insets were compared via Student's t-test (IEI t=1.161, df=66, $p = 0.$ 0.2499). (**j**) Model and proposed mechanism of rescue for LOF patients ameliorating loss of wildtype isoforms. Data represented as mean ± sem. n reported as n (samples)/d (donors) | independent batches.

		CONTROL				5'-DEL		3'-DEL		Genotype
										Data Point Color
Reference	Experiment	553-3	2607-4	3182-3	690-2	972-5	973-5	581-5	641-6	Donor Cell Line-Clone
Fig. 1 & ED Fig. S2	iGLUT/ iGABA generation	✓	✓	✓	✓	✓	✓	✓	✓	
	Immunostaining	✓	✓							
	Case/Control RNASeq	✓	✓			✓	✓	✓	✓	
Fig. 2 & ED Fig. S3	Case/Control MEA iGLUT	✓	✓			✓	✓	✓	✓	
	Case/Control MEA iGABA	✓	✓	✓	✓	✓	✓	✓	✓	
	Patch-Clamp iGLUT (Excitability)	✓	✓			✓	✓	✓	✓	
	Patch-Clamp iGABA (Excitability)	✓	✓			✓	✓	✓	✓	
ED Fig. S4	KCC2 MEA (GABAZine)			✓	✓					
Fig. 3	Patch-Clamp iGLUT (Neurotransmitter release)	✓	✓	✓	✓	✓	✓	✓	✓	
Fig. 3	Patch-Clamp iGABA (Neurotransmitter release)	✓	✓			✓	✓	✓	✓	
ED Fig S5	TTX Experiments iGLUT	✓	✓			✓	✓	✓	✓	
ED Fig S5	TTX Experiments iGABA	✓	✓		✓	✓	✓	✓	✓	
Fig. 4, ED Fig. S6 & S7	Organoid generation	✓	✓			✓	✓	✓	✓	
	Organoid characterization	✓	✓			✓	✓	✓	✓	
	Organoid rosette imaging	✓	✓			✓	✓	✓	✓	
	Organoid single cell sequencing	✓*	✓			✓	✓	✓	✓	
Fig. 5 & ED FigS8.	shRNA testing iGLUT-WT	✓	✓	✓	✓					
	shRNA patch-clamp iGLUT-WT				✓					
	shRNA testing iGABA-WT	✓	✓	✓	✓					
	shRNA patch-clamp iGABA-WT		✓	✓	✓					
	shRNA testing iGLUT-MT							✓	✓	
	shRNA patch-clamp iGLUT-MT							✓		
	shRNA testing iGABA-MT							✓	✓	
	shRNA patch-clamp iGABA-MT							✓		
	shRNA RNASeq			✓	✓			✓		
Fig. 6	Beta-Estradiol				✓	✓	✓			
Fig. 6	Anti-sense Oligos							✓	✓	

Extended Data Figure 1: *Specific cell lines used in each experiment throughout this study.* Reference table of all cell lines-clones used per experiment with corresponding data point colors. Check marks indicate inclusion for experiments, *represents dropped donor due to failed QC.

a

	iGLUT 5'-Del		iGLUT 3'-Del		iGABA 5'-Del		iGABA 3'-Del	
	Overlapped DEGs with risk genes	Overlapped DEGs with risk genes & in SIGNOR database	Overlapped DEGs with risk genes	Overlapped DEGs with risk genes & in SIGNOR database	Overlapped DEGs with risk genes	Overlapped DEGs with risk genes & in SIGNOR database	Overlapped DEGs with risk genes	Overlapped DEGs with risk genes & in SIGNOR database
ASD	11	**7**	4	**0**	3	**1**	6	**2**
BP	16	**9**	3	**1**	2	**1**	5	**1**
SCZ	26	**14**	10	**1**	9	**3**	14	**3**
Total	37	**22**	12	**2**	9	**3**	18	**4**

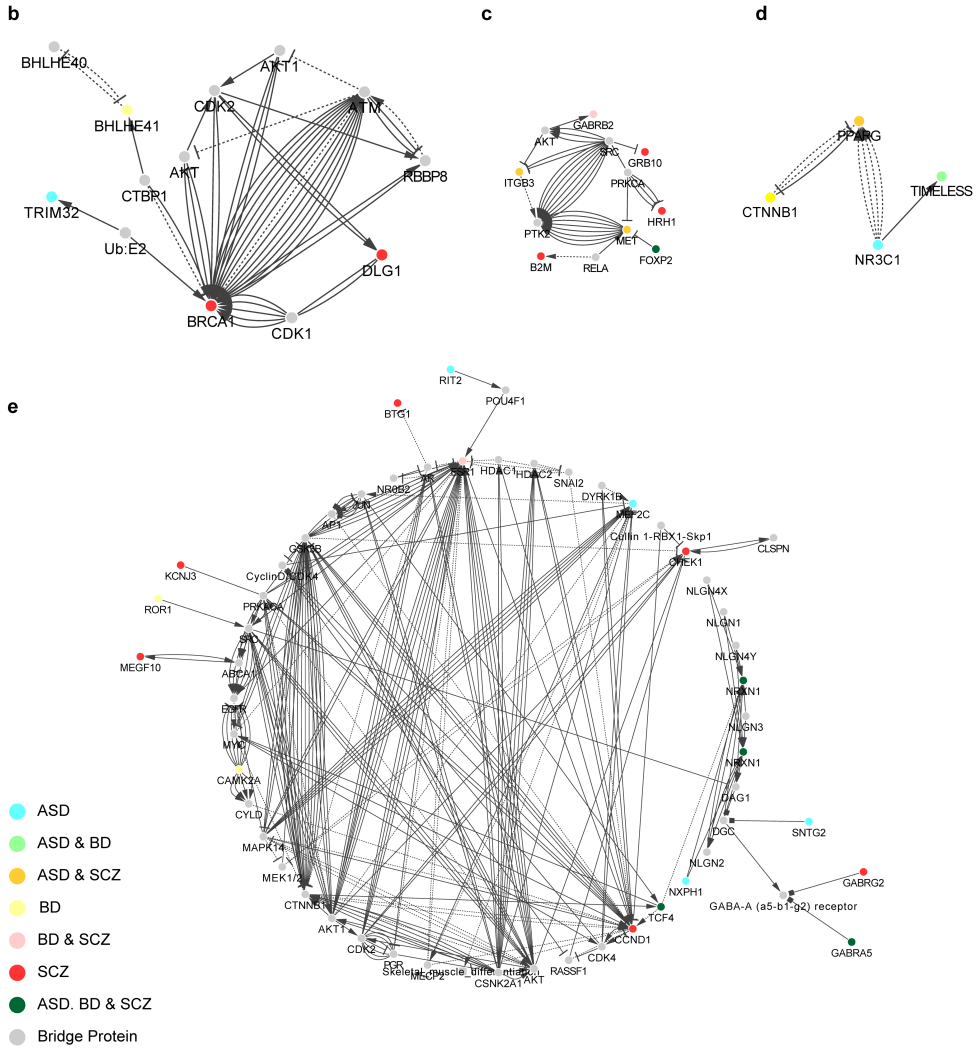

Extended Data Figure 2: *Extended transcriptomics analysis on disease risk associated genes.* (**a**) Summary table of overlapping DEGs with risk enrichments across publicly curated datasets for autism (ASD), bipolar disorder (BD) and schizophrenia. Interaction maps of risk genes for (**b**) 3'-Del iGLUT, (**c**) 3'-Del iGABA, (**d**) 5'-Del iGABA and (**e**) 5'-iGLUT. Sample information correspond to Fig. 1

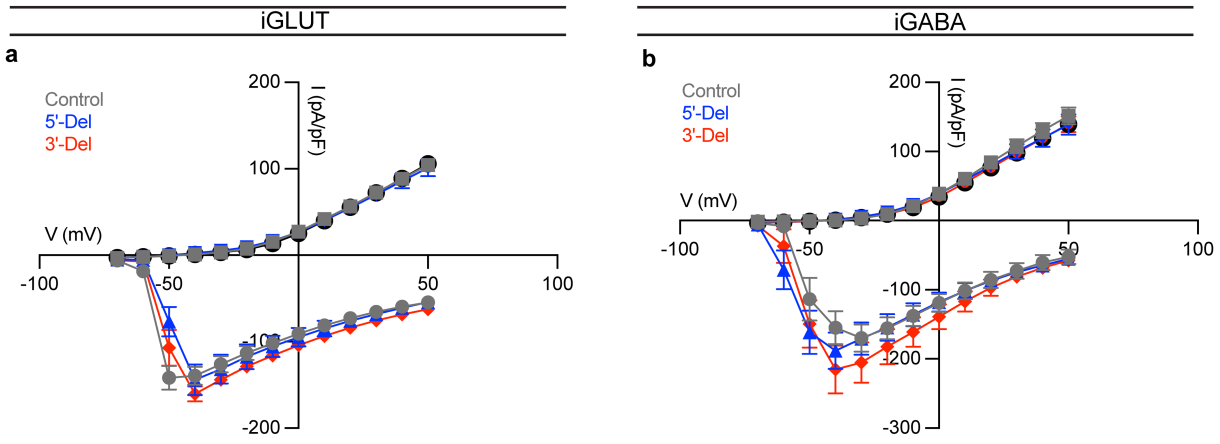

Extended Data Figure 3: *Extended data excitable properties of 5'-Del and 3'-Del neurons.* Voltage-gated potassium and channel kinetics across genotypes for (**a**) iGLUT and (**b**) iGABA neurons, sample information correspond Fig. 2. Data represented as mean ± sem.

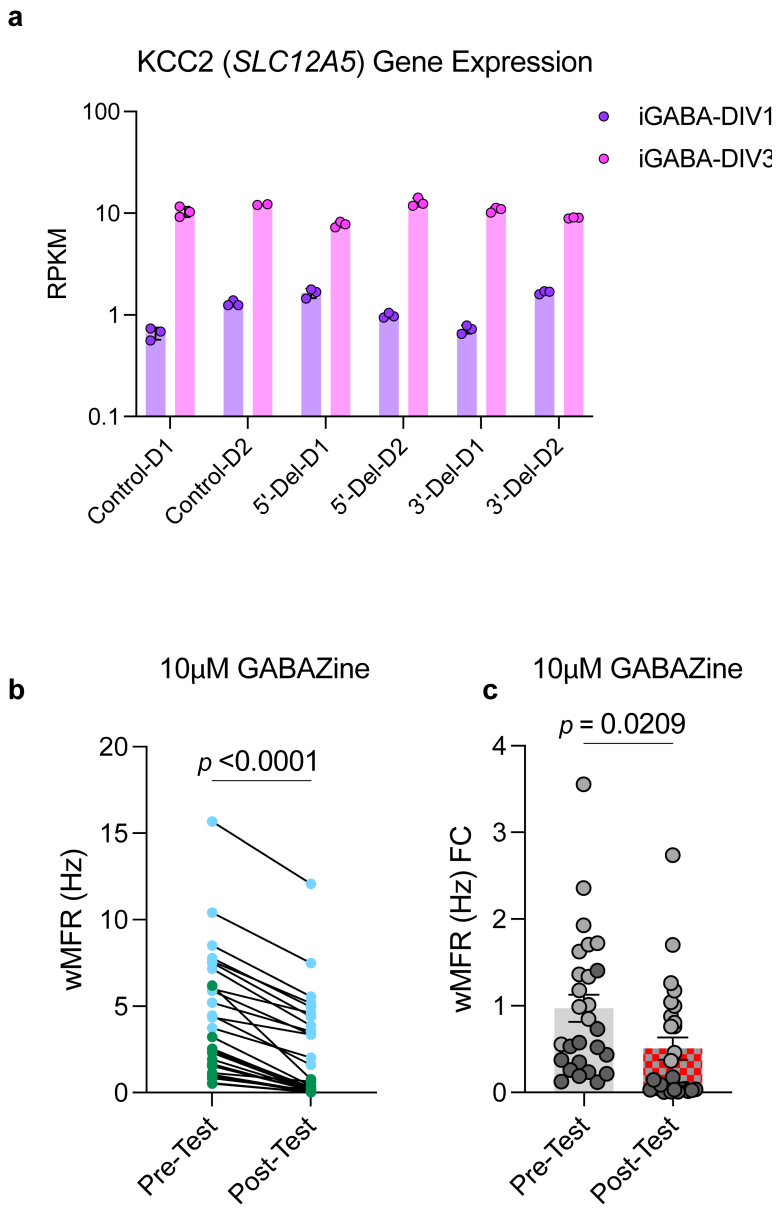

Extended Data Figure 4: *Extended KCC2 related data from immature GABA neurons.* (**a**) Transcriptomic comparison of *SLC12A5* expression across DIV14 and DIV35 RNASeq timepoints sample information correspond Fig. 1 (iGABA), compared via mixed effects model-time ($F_{1, 28}$ = 499.1 p <0.0001). (**b,c**) MEA tests from pre- and post- treatment of 10µM GABAzine. (n/d = 28/2 | 1 representative batch) compared via paired student's t-test for time-linked comparison (t=9.739, df=27; p < 0.0001) and unpaired student's t-test for pre/post activity foldchange (t=2.380, df=54; 0.0209). Data represented as mean ± sem. n reported as n (samples)/d (donors) | independent batches.

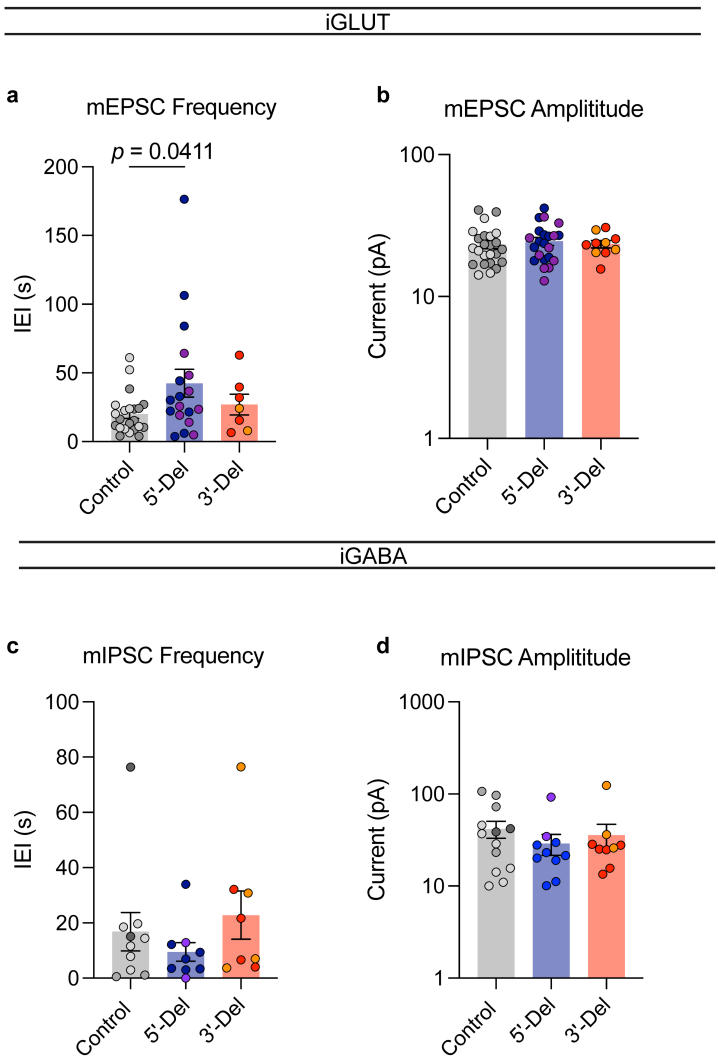

935

936 **Extended Data Figure 5:** *Miniature neurotransmitter release (+TTX) from iGLUT and iGABA*
937 *neurons.* Comparative GLUT mEPSC kinetics of (**a**) IEI (n/d: Control = 22/2; 5'-Del = 18/2; 3'-Del
938 = 7/2 | 4 batches) compared via 1-way ANOVA, with Dunnett's test ($F_{2, 44}$ = 2.880; 5'-Del p =
939 0.0411, 3'-Del p = 0.8229, and (**b**) amplitude size (n/d: Control = 24/2; 5'-Del = 22/2; 3'-Del = 10/2
940 | 4 batches) compared via 1-way ANOVA, with Dunnett's test ($F_{2, 53}$ = 0.1996; 5'-Del p = 0.7806,
941 3'-Del p = 0.9972). (**c**) Comparative iGABA mIPSC kinetics of IEI (n/d: Control = 10/2; 5'-Del =
942 9/2; 3'-Del = 8/2 | 3 batches) compared via 1-way ANOVA, with Dunnett's test ($F_{2, 24}$ = 0.9632; 5'-
943 Del p = 0.6452, 3'-Del p = 0.7565, and (**d**) amplitude size (n/d: Control = 13/2; 5'-Del = 10/2; 3'-
944 Del = 9/2 | 3 batches) compared via 1-way ANOVA, with Dunnett's test ($F_{2, 29}$ = 0.5097; 5'-Del p =
945 0.5141, 3'-Del p = 0.8618). Data represented as mean ± sem. n reported as n (samples)/d
946 (donors) | independent batches.

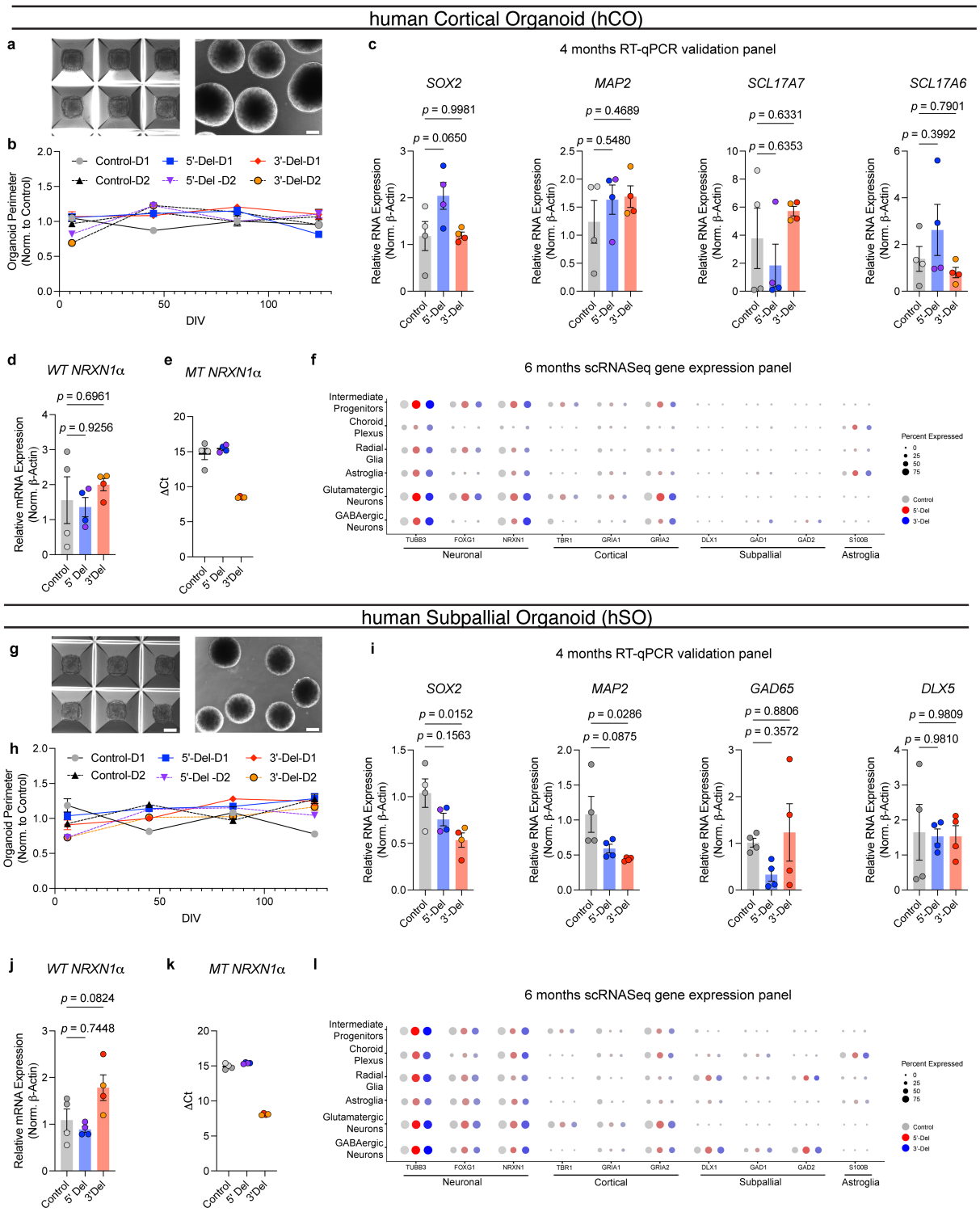

Extended Data Figure 6: *Extended data on human organoid generation and characterization.* (**a,g**) Representative images of hiPSC aggregation and immature spheroids post dislodging. (**b,h**) Normalized organoid perimeters over time (relative to averaged control) for hCO (n/d: Control = 136/2; 5'-Del = 128/2; 3'-Del = 150/2 | 2 batches) and hSO (n/d: Control = 118/2; 5'-Del = 92/2;

952 3'-Del = 120/2 | 2 batches). (**c**) hCO RT-qPCR results from 4-month organoids of genes for
953 pluripotency, neuronal, and cell-type specific markers (n/d: Control = 4/2; 5'-Del = 4/2; 3'-Del =
954 4/2 | 2 batches), compared via 1-way ANOVA, with Dunnett's test (*SOX2* $F_{2, 9} = 3.921$, 5'-Del p =
955 0.065, 3'-Del $p = 0.9981$; *MAP2AB* $F_{2, 9} = 0.7201$, 5'-Del $p = 0.5479$, 3'-Del $p = 0.4688$; *vGLUT1*
956 $F_{2, 9} = 1.594$, 5'-Del $p = 0.6353$, 3'-Del $p = 0.6331$; *vGLUT2* $F_{2, 9} = 1.710$, 5'-Del $p = 0.3992$, 3'-Del
957 $p = 0.7901$). (**d,e**) hCO RT-qPCR results of *NRXN1* WT and MT expression (n/d: Control = 4/2;
958 5'-Del = 4/2; 3'-Del = 4/2 | Representative batch) compared via 1-way ANOVA, with Dunnett's test
959 (*NRXN1-WT* $F_{2, 9} = 0.5873$, 5'-Del $p = 0.9256$, 3'-Del $p = 0.6961$) (**f**) Comprehensive gene
960 expression panel across sub-clusters of hCO samples across neuronal, cortical, subpallial and
961 astroglia markers. (**i**) hSO RT-qPCR results from 4-month organoids of genes for pluripotency,
962 neuronal, and cell-type specific markers (n/d: Control = 4/2; 5'-Del = 4/2; 3'-Del = 4/2 | 2 batches),
963 compared via 1-way ANOVA, with Dunnett's test (*SOX2* $F_{2, 9} = 5.683$, 5'-Del $p = 0.1563$, 3'-Del p
964 = 0.0152; *MAP2AB* $F_{2, 9} = 4.800$, 5'-Del $p = 0.0875$, 3'-Del $p = 0.0285$; *GAD65* $F_{2, 9} = 1.641$, 5'-
965 Del p 0.3573, 3'-Del $p = 0.8806$; *DLX5* $F_{2, 9} = 0.01755$, 5'-Del $p = 0.981$, 3'-Del $p = 0.9809$). (**j,k**)
966 hSO RT-qPCR results of *NRXN1* WT and MT expression (n/d: Control = 4/2; 5'-Del = 4/2; 3'-Del
967 = 4/2 | Representative batch) compared via 1-way ANOVA, with Dunnett's test (*NRXN1-WT* $F_{2, 9}$
968 = 4.818, 5'-Del $p = 0.7447$, 3'-Del $p = 0.0824$) (**l**) Comprehensive gene expression panel across
969 sub-clusters of hSO samples across neuronal, cortical, subpallial and astroglia markers. Data
970 corresponds to Fig 4. Data represented as mean ± sem. n (samples)/d (donors) | independent
971 batches.
972

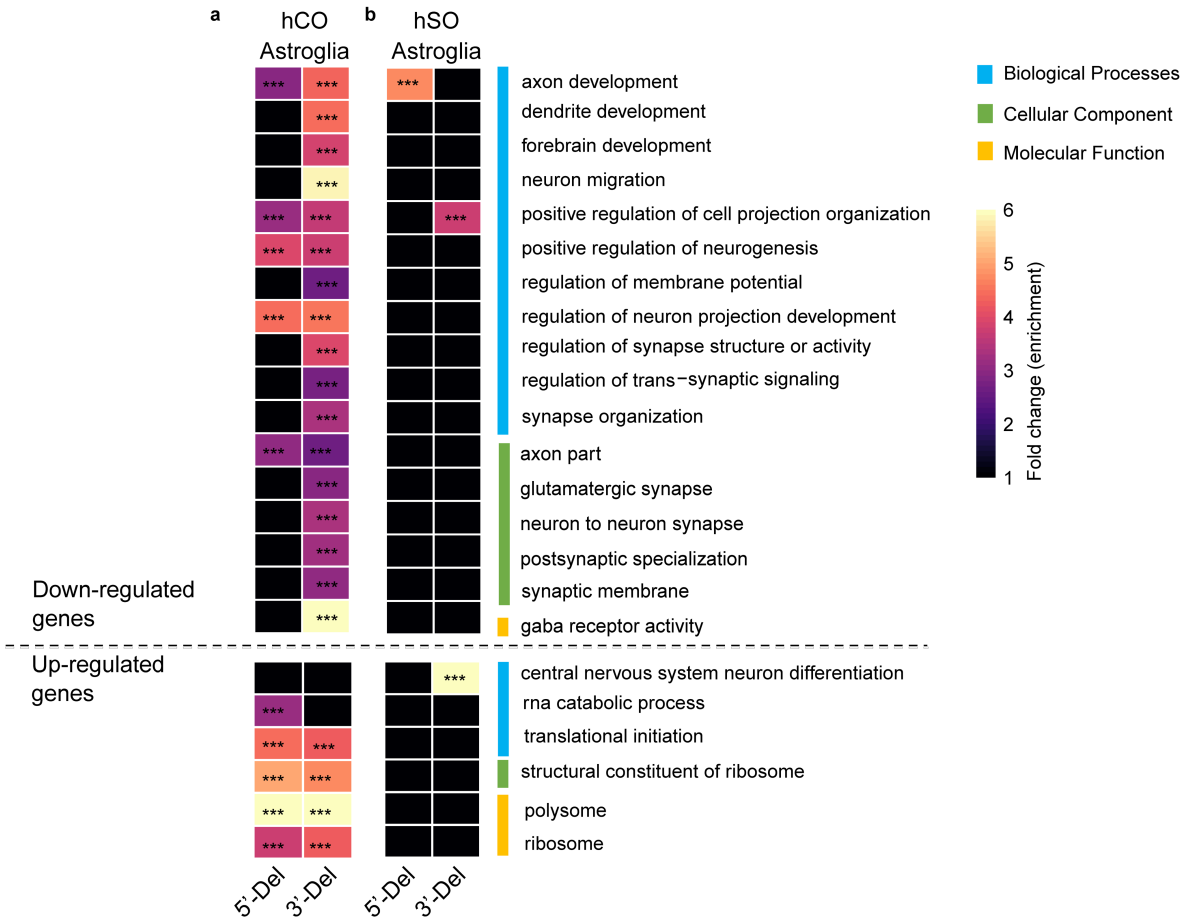

Extended Data Figure 7: *Extended analysis on astroglia subclusters from hCO and hSOs.* (a) hCO subcluster and (b) hCO subcluster GO analysis of overlapped terms with hCO-glutamatergic and hSO-GABAergic enrichments. *P < 0.05, **P < 0.01, ***P <0.001, Wilcoxon's rank sum test, FDR = 0.05.

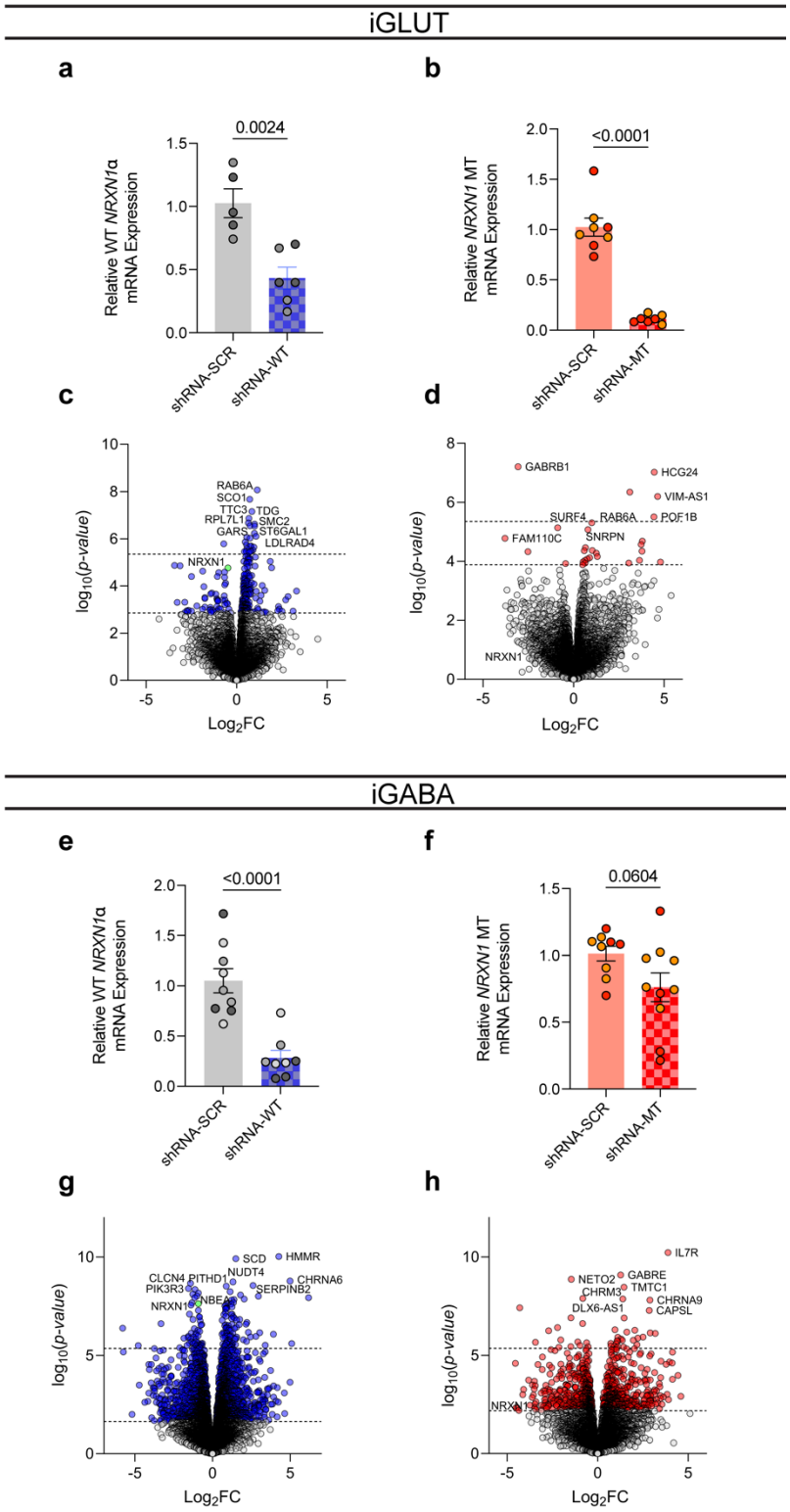

979 **Extended Data Figure 8:** *shRNA knockdown validation on representative batches.* (a) iGLUT
980 RT-qPCR of shRNA knockdown on WT *NRXN1* (n/d: shNT = 5/2; shWT = 6/2) compared via two-

tailed t-test (t=4.186, df=9, p = 0.0024), and (b) MT *NRXN1* (n/d: shNT = 8/2; shMT = 7/2) compared via two-tailed t-test (t=9.342, df=13, p < 0.0001). (c,d) iGLUT RNASeq DEG plots of WT (n/d: shNT = 3/1; shWT = 3/1) and MT (n/d: shNT = 2/1; shMT = 2/1) knockdowns performed in isogenic analyses. (a) iGABA RT-qPCR of shRNA knockdown on WT *NRXN1* (n/d: shNT = 8/3; shWT = 8/3) compared via two-tailed t-test (t=5.294, df=15, p < 0.0001), and (b) MT *NRXN1* (n/d: shNT = 9/2; shMT = 10/2) compared via two-tailed t-test (t=2.011, df=17, p = 0.0604). (c,d) iGABA RNASeq DEG plots of WT (n/d: shNT = 3/1; shWT = 3/1) and MT (n/d: shNT = 2/1; shMT = 2/1 | 2-4 wells pooled across 2 batches) knockdowns performed in isogenic analyses. Data represented as mean ± sem. n (samples)/d (donors).

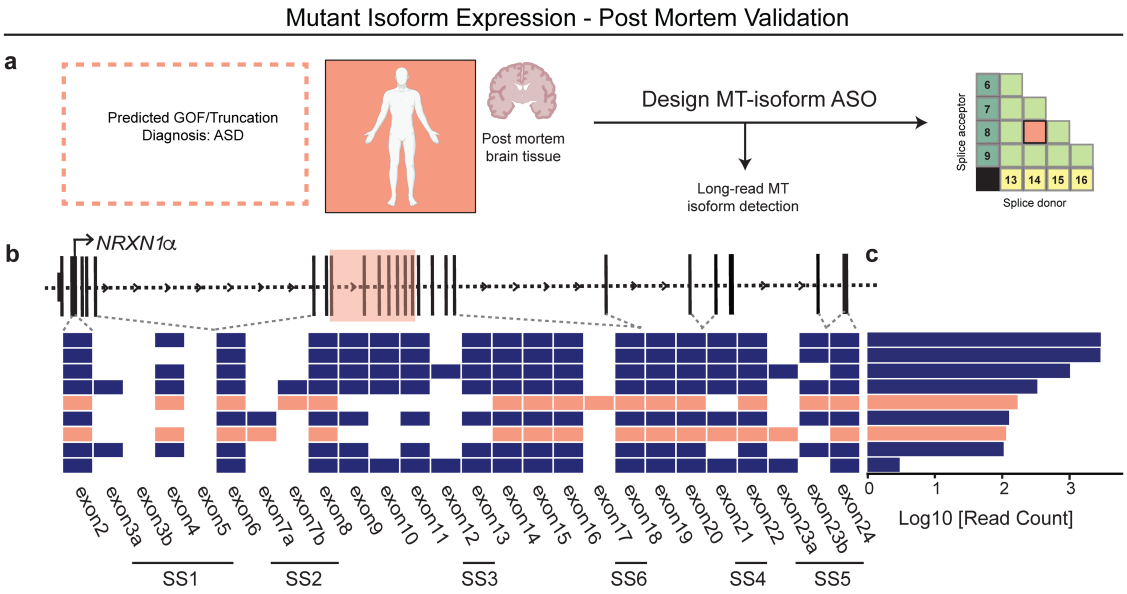

Extended Data Figure 9: *In-vivo validation of MT isoform expression from an unrelated autism NRXN1$^{+/-}$ patient.* (a) Schematic of novel NRXN1 autism patient, and GOF therapeutic targeting pipeline, with (b) schematic of the *NRXN1α* isoform structures, with each row representing a unique *NRXN1α* isoform and each column representing a *NRXN1* exon. The colored isoforms (navy, wildtype; peach, patient-specific) are spliced into the transcript while the blank exons are spliced out. (c) The abundance of each *NRXN1α* isoform by sample.

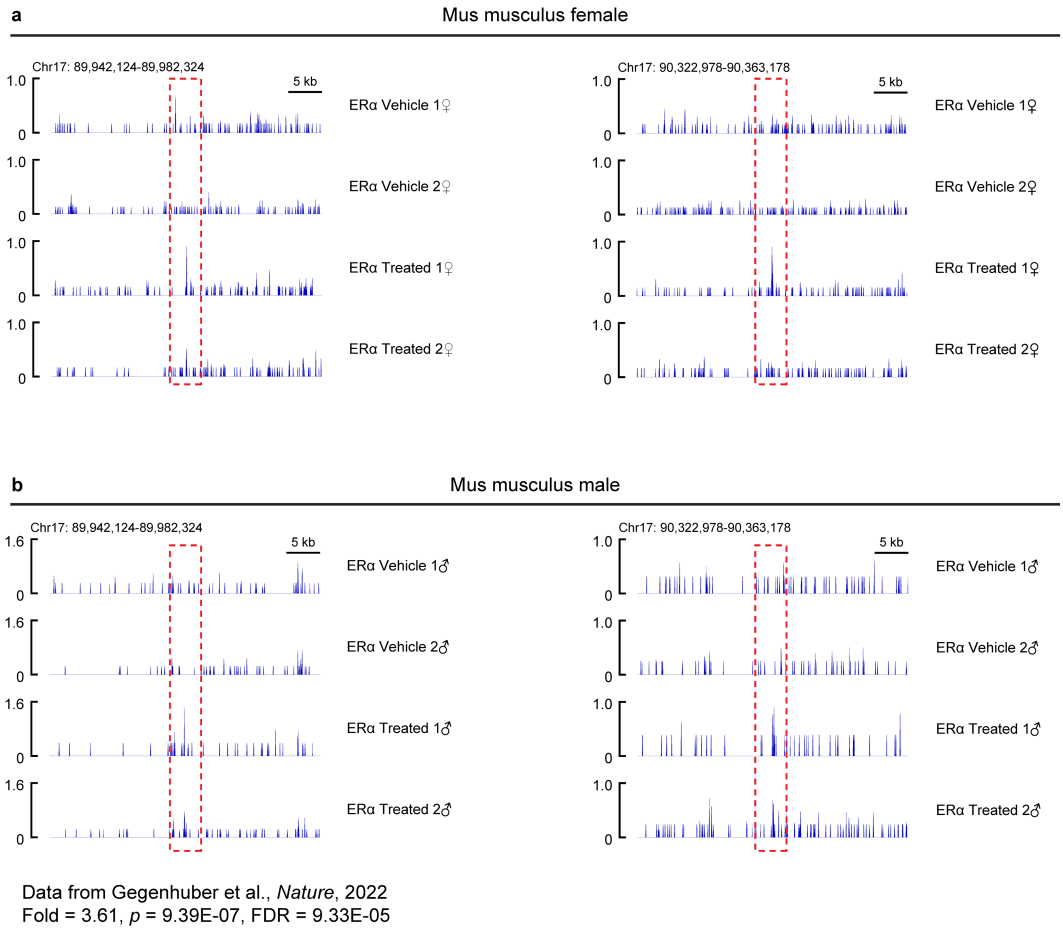

Extended Data Figure 10: *ChIP-seq enrichment of ER1 binding at NRXN1 loci in rodent brain.* (a) Female and (b) male mus musculus ChIP tracts of *NRXN1* locus, with red dashed areas highlighting binding enrichment across vehicle and estradiol treated mice.

1003 **References**

1004 1 Sudhof, T. C. Synaptic Neurexin Complexes: A Molecular Code for the Logic of Neural
1005 Circuits. *Cell* **171**, 745-769 (2017). https://doi.org:10.1016/j.cell.2017.10.024
1006 2 de Wit, J. & Ghosh, A. Specification of synaptic connectivity by cell surface interactions.
1007 *Nat Rev Neurosci* **17**, 22-35 (2016). https://doi.org:10.1038/nrn.2015.3
1008 3 Yang, X. *et al.* Widespread Expansion of Protein Interaction Capabilities by Alternative
1009 Splicing. *Cell* **164**, 805-817 (2016). https://doi.org:10.1016/j.cell.2016.01.029
1010 4 Schreiner, D. *et al.* Targeted combinatorial alternative splicing generates brain region-
1011 specific repertoires of neurexins. *Neuron* **84**, 386-398 (2014).
1012 https://doi.org:10.1016/j.neuron.2014.09.011
1013 5 Fuccillo, M. V. *et al.* Single-Cell mRNA Profiling Reveals Cell-Type-Specific Expression of
1014 Neurexin Isoforms. *Neuron* **87**, 326-340 (2015).
1015 https://doi.org:10.1016/j.neuron.2015.06.028
1016 6 Marshall, C. R. *et al.* Contribution of copy number variants to schizophrenia from a
1017 genome-wide study of 41,321 subjects. *Nat Genet* **49**, 27-35 (2017).
1018 https://doi.org:10.1038/ng.3725
1019 7 Matsunami, N. *et al.* Identification of rare recurrent copy number variants in high-risk
1020 autism families and their prevalence in a large ASD population. *PLoS One* **8**, e52239
1021 (2013). https://doi.org:10.1371/journal.pone.0052239
1022 8 Moller, R. S. *et al.* Exon-disrupting deletions of NRXN1 in idiopathic generalized epilepsy.
1023 *Epilepsia* **54**, 256-264 (2013). https://doi.org:10.1111/epi.12078
1024 9 Ching, M. S. *et al.* Deletions of NRXN1 (neurexin-1) predispose to a wide spectrum of
1025 developmental disorders. *Am J Med Genet B Neuropsychiatr Genet* **153B**, 937-947
1026 (2010). https://doi.org:10.1002/ajmg.b.31063
1027 10 Huang, A. Y. *et al.* Rare Copy Number Variants in NRXN1 and CNTN6 Increase Risk for
1028 Tourette Syndrome. *Neuron* **94**, 1101-1111 e1107 (2017).
1029 https://doi.org:10.1016/j.neuron.2017.06.010
1030 11 Grayton, H. M., Missler, M., Collier, D. A. & Fernandes, C. Altered social behaviours in
1031 neurexin 1alpha knockout mice resemble core symptoms in neurodevelopmental
1032 disorders. *PLoS One* **8**, e67114 (2013). https://doi.org:10.1371/journal.pone.0067114
1033 12 Pak, C. *et al.* Human Neuropsychiatric Disease Modeling using Conditional Deletion
1034 Reveals Synaptic Transmission Defects Caused by Heterozygous Mutations in NRXN1.
1035 *Cell stem cell* **17**, 316-328 (2015). https://doi.org:10.1016/j.stem.2015.07.017

1036 13 Pak, C. *et al.* Cross-platform validation of neurotransmitter release impairments in
1037 schizophrenia patient-derived NRXN1-mutant neurons. *Proc Natl Acad Sci U S A* **118**
1038 (2021). https://doi.org:10.1073/pnas.2025598118
1039 14 Flaherty, E. *et al.* Neuronal impact of patient-specific aberrant NRXN1alpha splicing. *Nat*
1040 *Genet* **51**, 1679-1690 (2019). https://doi.org:10.1038/s41588-019-0539-z
1041 15 Boxer, E. E. & Aoto, J. Neurexins and their ligands at inhibitory synapses. *Front Synaptic*
1042 *Neurosci* **14**, 1087238 (2022). https://doi.org:10.3389/fnsyn.2022.1087238
1043 16 Gomez, A. M., Traunmüller, L. & Scheiffele, P. Neurexins: molecular codes for shaping
1044 neuronal synapses. *Nature Reviews Neuroscience* **22**, 137-151 (2021).
1045 https://doi.org:10.1038/s41583-020-00415-7
1046 17 Taoufik, E., Kouroupi, G., Zygogianni, O. & Matsas, R. Synaptic dysfunction in
1047 neurodegenerative and neurodevelopmental diseases: an overview of induced pluripotent
1048 stem-cell-based disease models. *Open Biology* **8**, 180138 (2018).
1049 https://doi.org:10.1098/rsob.180138
1050 18 Ho, S. M. *et al.* Rapid Ngn2-induction of excitatory neurons from hiPSC-derived neural
1051 progenitor cells. *Methods* **101**, 113-124 (2016).
1052 https://doi.org:10.1016/j.ymeth.2015.11.019
1053 19 Barretto, N. *et al.* ASCL1- and DLX2-induced GABAergic neurons from hiPSC-derived
1054 NPCs. *J Neurosci Methods* **334**, 108548 (2020).
1055 https://doi.org:10.1016/j.jneumeth.2019.108548
1056 20 Zhang, Y. *et al.* Rapid single-step induction of functional neurons from human pluripotent
1057 stem cells. *Neuron* **78**, 785-798 (2013). https://doi.org:10.1016/j.neuron.2013.05.029
1058 21 Schrode, N. *et al.* Synergistic effects of common schizophrenia risk variants. *Nat Genet*
1059 **51**, 1475-1485 (2019). https://doi.org:10.1038/s41588-019-0497-5
1060 22 Yang, N. *et al.* Generation of pure GABAergic neurons by transcription factor
1061 programming. *Nat Methods* (2017). https://doi.org:10.1038/nmeth.4291
1062 23 Seah, C. *et al.* Modeling gene x environment interactions in PTSD using human neurons
1063 reveals diagnosis-specific glucocorticoid-induced gene expression. *Nat Neurosci* **25**,
1064 1434-1445 (2022). https://doi.org:10.1038/s41593-022-01161-y
1065 24 Lo Surdo, P. *et al.* SIGNOR 3.0, the SIGnaling network open resource 3.0: 2022 update.
1066 *Nucleic Acids Res* **51**, D631-d637 (2023). https://doi.org:10.1093/nar/gkac883
1067 25 Virtanen, M. A., Uvarov, P., Mavrovic, M., Poncer, J. C. & Kaila, K. The Multifaceted Roles
1068 of KCC2 in Cortical Development. *Trends in neurosciences* **44**, 378-392 (2021).
1069 https://doi.org:https://doi.org/10.1016/j.tins.2021.01.004

1070 26 Sohal, V. S. & Rubenstein, J. L. R. Excitation-inhibition balance as a framework for
1071 investigating mechanisms in neuropsychiatric disorders. *Mol Psychiatry* **24**, 1248-1257
1072 (2019). https://doi.org:10.1038/s41380-019-0426-0
1073 27 Schafer, S. T. *et al.* Pathological priming causes developmental gene network
1074 heterochronicity in autistic subject-derived neurons. *Nat Neurosci* **22**, 243-255 (2019).
1075 https://doi.org:10.1038/s41593-018-0295-x
1076 28 Birey, F. *et al.* Assembly of functionally integrated human forebrain spheroids. *Nature* **545**,
1077 54-59 (2017). https://doi.org:10.1038/nature22330
1078 29 Yoon, S. J. *et al.* Reliability of human cortical organoid generation. *Nat Methods* **16**, 75-
1079 78 (2019). https://doi.org:10.1038/s41592-018-0255-0
1080 30 Khan, T. A. *et al.* Neuronal defects in a human cellular model of 22q11.2 deletion
1081 syndrome. *Nat Med* **26**, 1888-1898 (2020). https://doi.org:10.1038/s41591-020-1043-9
1082 31 Willsey, H. R. *et al.* Parallel in vivo analysis of large-effect autism genes implicates cortical
1083 neurogenesis and estrogen in risk and resilience. *Neuron* **109**, 1409 (2021).
1084 https://doi.org:10.1016/j.neuron.2021.03.030
1085 32 Roberts, T. C., Langer, R. & Wood, M. J. A. Advances in oligonucleotide drug delivery.
1086 *Nature Reviews Drug Discovery* **19**, 673-694 (2020). https://doi.org:10.1038/s41573-020-
1087 0075-7
1088 33 Gegenhuber, B., Wu, M. V., Bronstein, R. & Tollkuhn, J. Gene regulation by gonadal
1089 hormone receptors underlies brain sex differences. *Nature* **606**, 153-159 (2022).
1090 https://doi.org:10.1038/s41586-022-04686-1
1091 34 Sebastian, R. *et al.* Schizophrenia-associated NRXN1 deletions induce developmental-
1092 timing- and cell-type-specific vulnerabilities in human brain organoids. *Nature*
1093 *Communications* **14**, 3770 (2023). https://doi.org:10.1038/s41467-023-39420-6
1094 35 Zeng, L. *et al.* Functional impacts of NRXN1 knockdown on neurodevelopment in stem
1095 cell models. *PLoS One* **8**, e59685 (2013). https://doi.org:10.1371/journal.pone.0059685
1096 36 Birtele, M. *et al.* The autism-associated gene SYNGAP1 regulates human cortical
1097 neurogenesis. *bioRxiv*, 2022.2005.2010.491244 (2022).
1098 https://doi.org:10.1101/2022.05.10.491244
1099 37 Trotter, J. H. *et al.* Astrocytic Neurexin-1 Orchestrates Functional Synapse Assembly.
1100 *BioRxiv* (2020). https://doi.org:10.1101/2020.08.21.262097
1101 38 Ingusci, S., Verlengia, G., Soukupova, M., Zucchini, S. & Simonato, M. Gene Therapy
1102 Tools for Brain Diseases. *Frontiers in pharmacology* **10** (2019).
1103 https://doi.org:10.3389/fphar.2019.00724

39 Brunet de Courssou, J.-B., Durr, A., Adams, D., Corvol, J.-C. & Mariani, L.-L. Antisense therapies in neurological diseases. *Brain* **145**, 816-831 (2022). https://doi.org:10.1093/brain/awab423

40 Yilmaz, C. *et al.* Neurosteroids as regulators of neuroinflammation. *Frontiers in Neuroendocrinology* **55**, 100788 (2019). https://doi.org:https://doi.org/10.1016/j.yfrne.2019.100788

41 National Academies of Sciences, E. & Medicine. *Sex Differences in Brain Disorders: Emerging Transcriptomic Evidence: Proceedings of a Workshop*. (The National Academies Press, 2021).

42 Jack, A. *et al.* A neurogenetic analysis of female autism. *Brain* **144**, 1911-1926 (2021). https://doi.org:10.1093/brain/awab064

43 Werling, D. M. The role of sex-differential biology in risk for autism spectrum disorder. *Biol Sex Differ* **7**, 58 (2016). https://doi.org:10.1186/s13293-016-0112-8

44 Hoffman, E. J. *et al.* Estrogens Suppress a Behavioral Phenotype in Zebrafish Mutants of the Autism Risk Gene, CNTNAP2. *Neuron* **89**, 725-733 (2016). https://doi.org:10.1016/j.neuron.2015.12.039

45 McCarthy, M. M. Estradiol and the developing brain. *Physiol Rev* **88**, 91-124 (2008). https://doi.org:10.1152/physrev.00010.2007

46 Woolley, C. S. Acute Effects of Estrogen on Neuronal Physiology. *Annual Review of Pharmacology and Toxicology* **47**, 657-680 (2007). https://doi.org:10.1146/annurev.pharmtox.47.120505.105219

47 Lin, H. C. *et al.* NGN2 induces diverse neuron types from human pluripotency. *Stem Cell Reports* **16**, 2118-2127 (2021). https://doi.org:10.1016/j.stemcr.2021.07.006

48 Zafra, F. & Piniella, D. Proximity labeling methods for proteomic analysis of membrane proteins. *Journal of Proteomics* **264**, 104620 (2022). https://doi.org:https://doi.org/10.1016/j.jprot.2022.104620

49 Bell, J. Stratified medicines: towards better treatment for disease. *Lancet* **383 Suppl 1**, S3-5 (2014). https://doi.org:10.1016/s0140-6736(14)60115-x

50 Tsimberidou, A. M. *et al.* Molecular tumour boards — current and future considerations for precision oncology. *Nature Reviews Clinical Oncology* **20**, 843-863 (2023). https://doi.org:10.1038/s41571-023-00824-4

51 Zhang, H., Colclough, K., Gloyn, A. L. & Pollin, T. I. Monogenic diabetes: a gateway to precision medicine in diabetes. *The Journal of Clinical Investigation* **131** (2021). https://doi.org:10.1172/JCI142244

1138 52 Sullivan, P. F. & Geschwind, D. H. Defining the Genetic, Genomic, Cellular, and
1139 Diagnostic Architectures of Psychiatric Disorders. *Cell* **177**, 162-183 (2019).
1140 https://doi.org:10.1016/j.cell.2019.01.015
1141 53 Gerasimavicius, L., Livesey, B. J. & Marsh, J. A. Loss-of-function, gain-of-function and
1142 dominant-negative mutations have profoundly different effects on protein structure. *Nature*
1143 *Communications* **13**, 3895 (2022). https://doi.org:10.1038/s41467-022-31686-6
1144 54 Wang, L. *et al.* Analyses of the autism-associated neuroligin-3 R451C mutation in human
1145 neurons reveal a gain-of-function synaptic mechanism. *Molecular psychiatry* (2022).
1146 https://doi.org:10.1038/s41380-022-01834-x
1147 55 Pinggera, A. *et al.* New gain-of-function mutation shows CACNA1D as recurrently mutated
1148 gene in autism spectrum disorders and epilepsy. *Hum Mol Genet* **26**, 2923-2932 (2017).
1149 https://doi.org:10.1093/hmg/ddx175
1150 56 Clark, M. B. *et al.* Long-read sequencing reveals the complex splicing profile of the
1151 psychiatric risk gene CACNA1C in human brain. *Molecular psychiatry* **25**, 37-47 (2020).
1152 57 Brunklaus, A. *et al.* Gene variant effects across sodium channelopathies predict function
1153 and guide precision therapy. *Brain* **145**, 4275-4286 (2022).
1154 https://doi.org:10.1093/brain/awac006
1155 58 Sanders, S. J. *et al.* Progress in Understanding and Treating SCN2A-Mediated Disorders.
1156 *Trends in neurosciences* **41**, 442-456 (2018).
1157 https://doi.org:https://doi.org/10.1016/j.tins.2018.03.011
1158 59 Kim, G., Gautier, O., Tassoni-Tsuchida, E., Ma, X. R. & Gitler, A. D. ALS Genetics: Gains,
1159 Losses, and Implications for Future Therapies. *Neuron* **108**, 822-842 (2020).
1160 https://doi.org:10.1016/j.neuron.2020.08.022
1161 60 Balendra, R. & Isaacs, A. M. C9orf72-mediated ALS and FTD: multiple pathways to
1162 disease. *Nat Rev Neurol* **14**, 544-558 (2018). https://doi.org:10.1038/s41582-018-0047-2
1163 61 Prakasam, R. *et al.* LSD1/PRMT6-targeting gene therapy to attenuate androgen receptor
1164 toxic gain-of-function ameliorates spinobulbar muscular atrophy phenotypes in flies and
1165 mice. *Nature Communications* **14**, 603 (2023). https://doi.org:10.1038/s41467-023-
1166 36186-9
1167 62 Chintalaphani, S. R., Pineda, S. S., Deveson, I. W. & Kumar, K. R. An update on the
1168 neurological short tandem repeat expansion disorders and the emergence of long-read
1169 sequencing diagnostics. *Acta Neuropathologica Communications* **9**, 98 (2021).
1170 https://doi.org:10.1186/s40478-021-01201-x

1171 63 Sloan, S. A., Andersen, J., Pasca, A. M., Birey, F. & Pasca, S. P. Generation and assembly
1172 of human brain region-specific three-dimensional cultures. *Nat Protoc* (2018).
1173 https://doi.org:10.1038/s41596-018-0032-7
1174 64 Nicolas, A. *et al.* Genome-wide Analyses Identify KIF5A as a Novel ALS Gene. *Neuron*
1175 **97**, 1268-1283 e1266 (2018). https://doi.org:10.1016/j.neuron.2018.02.027
1176 65 Dobin, A. *et al.* STAR: ultrafast universal RNA-seq aligner. *Bioinformatics* **29**, 15-21
1177 (2013). https://doi.org:10.1093/bioinformatics/bts635
1178 66 Liao, Y., Smyth, G. K. & Shi, W. featureCounts: an efficient general purpose program for
1179 assigning sequence reads to genomic features. *Bioinformatics* **30**, 923-930 (2014).
1180 https://doi.org:10.1093/bioinformatics/btt656
1181 67 Robinson, M. D., McCarthy, D. J. & Smyth, G. K. edgeR: a Bioconductor package for
1182 differential expression analysis of digital gene expression data. *Bioinformatics* **26**, 139-
1183 140 (2010). https://doi.org:10.1093/bioinformatics/btp616
1184 68 Hoffman, G. E. *et al.* Transcriptional signatures of schizophrenia in hiPSC-derived NPCs
1185 and neurons are concordant with post-mortem adult brains. *Nat Commun* **8**, 2225 (2017).
1186 https://doi.org:10.1038/s41467-017-02330-5
1187 69 Newman, A. M. *et al.* Determining cell type abundance and expression from bulk tissues
1188 with digital cytometry. *Nature biotechnology* **37**, 773-782 (2019).
1189 https://doi.org:10.1038/s41587-019-0114-2
1190 70 Hoffman, G. E. & Schadt, E. E. variancePartition: interpreting drivers of variation in
1191 complex gene expression studies. *BMC bioinformatics* **17**, 483 (2016).
1192 https://doi.org:10.1186/s12859-016-1323-z
1193 71 Ritchie, M. E. *et al.* limma powers differential expression analyses for RNA-sequencing
1194 and microarray studies. *Nucleic Acids Res* **43**, e47 (2015).
1195 https://doi.org:10.1093/nar/gkv007
1196 72 Bray, N. L., Pimentel, H., Melsted, P. & Pachter, L. Near-optimal probabilistic RNA-seq
1197 quantification. *Nature biotechnology* **34**, 525-527 (2016). https://doi.org:10.1038/nbt.3519
1198 73 De Marinis, I., Lo Surdo, P., Cesareni, G. & Perfetto, L. SIGNORApp: a Cytoscape 3
1199 application to access SIGNOR data. *Bioinformatics* **38**, 1764-1766 (2022).
1200 https://doi.org:10.1093/bioinformatics/btab865
1201 74 Stuart, T. *et al.* Comprehensive Integration of Single-Cell Data. *Cell* **177**, 1888-1902 e1821
1202 (2019). https://doi.org:10.1016/j.cell.2019.05.031

1203 75 Urresti, J. *et al.* Correction: Cortical organoids model early brain development disrupted
1204 by 16p11.2 copy number variants in autism. *Mol Psychiatry* **26**, 7581 (2021).
1205 https://doi.org:10.1038/s41380-021-01289-6
1206 76 Yang, X. *et al.* Identification and validation of genes affecting aortic lesions in mice. *J Clin*
1207 *Invest* **120**, 2414-2422 (2010). https://doi.org:10.1172/JCI42742
1208 77 Stefan, K. & Harbour, J. W. SparK: A Publication-quality NGS Visualization Tool. *bioRxiv*,
1209 845529 (2019). https://doi.org:10.1101/845529
1210